

***International Collaborations  
Activities on Disposal in  
Argillite R&D:  
Characterization Studies and  
Modeling Investigations***

**Fuel Cycle Research & Development**

***Prepared for  
U.S. Department of Energy  
Spent Fuel Waste Science  
and Technology***

***Carlos F. Jové Colón,  
Tuan A. Ho,  
Eric N. Coker,  
Carlos M. Lopez,  
Kristopher L. Kuhlman  
Amanda Sanchez,  
Melissa Mills,  
Jessica Kruichak  
Edward N. Matteo***

***Sandia National Laboratories  
May 7, 2020***

**SAND2021-6358 R**



**DISCLAIMER**

This information was prepared as an account of work sponsored by an agency of the U.S. Government. Neither the U.S. Government nor any agency thereof, nor any of their employees, makes any warranty, expressed or implied, or assumes any legal liability or responsibility for the accuracy, completeness, or usefulness, of any information, apparatus, product, or process disclosed, or represents that its use would not infringe privately owned rights. Reference herein to any specific commercial product, process, or service by trade name, trade mark, manufacturer, or otherwise, does not necessarily constitute or imply its endorsement, recommendation, or favoring by the U.S. Government or any agency thereof. The views and opinions of authors expressed herein do not necessarily state or reflect those of the U.S. Government or any agency thereof.

Sandia National Laboratories is a multimission laboratory managed and operated by National Technology and Engineering Solutions of Sandia, LLC, a wholly owned subsidiary of Honeywell International, Inc., for the U.S. Department of Energy's National Nuclear Security Administration under contract DE-NA-0003525.

This page is intentionally blank.

## ACKNOWLEDGEMENTS

The authors acknowledge our gratitude to Yifeng Wang (SNL), Charles R. Bryan (SNL), Jonny Rutqvist (LBNL), Liange Zheng (LBNL), Jens Birkholzer (LBNL), William Spezialetti (DOE NE-81), Prasad Nair (DOE NE-81), and Tim Gunter (DOE NE-81) for their helpful discussions and contributions on various topics covered in this report. Dr. Mark A. Rodriguez (SNL) and his staff conducted the *in situ* XRD analyses on FEBEX bentonite presented in this report. We also express our gratitude to Drs. Chen Gruber and Dr. David Kosson of Vanderbilt University for sharing their leaching test data and other technical information. Dr. Liange Zheng and Sharon Borglin of LBNL kindly provided the MX-80 bentonite samples and supporting technical information of the HotBENT column experiments. This work was supported by the DOE-NE SFWD office.

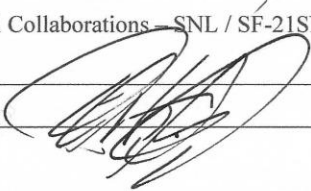
Revision 5  
01/15/2018

APPENDIX E  
NTRD DOCUMENT COVER SHEET<sup>1</sup>

Name/Title of Deliverable/Milestone/Revision No. International Collaborations Activities on Disposal in Argillite R&D: Characterization Studies and Modeling Investigations, M4SF-21SN010301082 / Rev.0

Work Package Title and Number Argillite International Collaborations - SNL / SF-21SN01030108

Work Package WBS Number 1.08.01.03.01

Responsible Work Package Manager Carlos F. Jove Colon   
(Name/Signature)

Date Submitted

Quality Rigor Level for Deliverable/Milestone <sup>2</sup>	<input type="checkbox"/> QRL-1 <input type="checkbox"/> Nuclear Data	<input type="checkbox"/> QRL-2	<input checked="" type="checkbox"/> QRL-3	<input type="checkbox"/> QRL-4 Lab QA Program <sup>3</sup>
--	---	--------------------------------	---	---


This deliverable was prepared in accordance with Sandia National Laboratory \_\_\_\_\_  
(Participant/National Laboratory Name)

QA program which meets the requirements of  
 DOE Order 414.1     NQA-1     Other

**This Deliverable was subjected to:**

- |   |  |
|---|--|
| <input checked="" type="checkbox"/> Technical Review                  | <input type="checkbox"/> Peer Review                       |
| <b>Technical Review (TR)</b>  | <b>Peer Review (PR)</b>                                    |
| <b>Review Documentation Provided</b>                                  | <b>Review Documentation Provided</b>                       |
| <input type="checkbox"/> Signed TR Report or,                         | <input type="checkbox"/> Signed PR Report or,              |
| <input type="checkbox"/> Signed TR Concurrence Sheet or,              | <input type="checkbox"/> Signed PR Concurrence Sheet or,   |
| <input checked="" type="checkbox"/> Signature of TR Reviewer(s) below | <input type="checkbox"/> Signature of PR Reviewer(s) below |

**Name and Signature of Reviewers**

Yifeng Wang (SNL)   
 Yifeng Wang (SNL) \_\_\_\_\_

**NOTE 1:** Appendix E should be filled out and submitted with the deliverable. Or, if the PICS:NE system permits, completely enter all applicable information in the PICS:NE Deliverable Form. The requirement is to ensure that all applicable information is entered either in the PICS:NE system or by using the NTRD Document Cover Sheet.

- In some cases there may be a milestone where an item is being fabricated, maintenance is being performed on a facility, or a document is being issued through a formal document control process where it specifically calls out a formal review of the document. In these cases, documentation (e.g., inspection report, maintenance request, work planning package documentation or the documented review of the issued document through the document control process) of the completion of the activity, along with the Document Cover Sheet, is sufficient to demonstrate achieving the milestone.

**NOTE 2:** If QRL 1, 2, or 3 is not assigned, then the QRL 4 box must be checked, and the work is understood to be performed using laboratory QA requirements. This includes any deliverable developed in conformance with the respective National Laboratory / Participant, DOE or NNSA-approved QA Program.

**NOTE 3:** If the lab has an NQA-1 program and the work to be conducted requires an NQA-1 program, then the QRL-1 box must be checked in the work Package and on the Appendix E cover sheet and the work must be performed in accordance with the Lab's NQA-1 program. The QRL-4 box should not be checked.

This page is intentionally blank

## Table of Contents

Table of Contents .....	7
Acronym List .....	10
I. Introduction .....	12
II. FEBEX-DP .....	14
III. Thermal (TGA/DSC) Analyses .....	17
IV. Transport-mechanical-chemical coupling effect during clay dehydration controlled by coordination number of interlayer ions .....	23
Method .....	25
Results .....	26
Conclusions from the MD Study .....	31
V. 1D Reactive-Transport Modeling of Sedimentary Rock Leaching Experiments .....	31
Introduction .....	31
Marl Rock Properties .....	32
Monolith leaching test (EPA Method 1315) .....	32
1D PFLOTRAN Reactive Transport Simulations .....	34
Preliminary Results and Discussion .....	35
VI. HotBENT Heated Column Experiment: Preliminary XRD Analysis of Post- Experiment Bentonite Samples .....	37
Preliminary XRD Analyses of Post-Experiment Bentonite Samples .....	39
VII. Conclusions .....	41
VIII. FY22 Work .....	42
IX. References .....	43

## Table of Figures

Figure 1. Schematic layout of the FEBEX “in-situ” field test after the first partial dismantling showing the configuration of heater #2 at the GTS URL. ....	15
Figure 2. Schematic configuration of sampling zones (indicated by vertical light blue bars) for the FEBEX-DP project. ....	15
Figure 3. Schematic diagram of sampling locations for the FEBEX-DP dismantling of section 49. ....	16
Figure 4. TGA, DTA, and DSC curves as a function of time for water adsorption/desorption cycles at 60°C for the <2 μm bentonite sample. ....	19
Figure 5. TGA and DSC curves as a function of time for water adsorption/desorption cycles at 60°C for the <75 μm bentonite sample. ....	20
Figure 9. Simulation system used to study the dehydration process of Na-MMT. The simulation box size is 150 × 31.06 × 200 Å <sup>3</sup> . ....	25
Figure 10. Mass loss (i.e., number of water molecules lost) as a function of simulation time . ....	27
Figure 11. Simulation snapshots demonstrate water transport pathway through an MMT interlayer during the dehydration process. ....	28
Figure 12. Coordination number of Na <sup>+</sup> ions and d-spacing as a function of time for first 5 ns and 50 ns simulations. ....	29
Figure 13. Mass loss, d-spacing, and water coordination number of Na <sup>+</sup> ion during the dehydration of 1W hydrated MMT at 30° and 60° C. ....	30
Figure 14. d-spacing and heat flow and mass as a function of time at 60 °C. ....	31
Figure 15. Bulk rock sample, epoxy-mounted sample used for 1315, and experimental setup for the 1315 test. ....	33
Figure 16. Mesh discretization of the solid and leaching solution domains along with dimensions of the rectangular domain. ....	34
Figure 17. Temporal change of pH and total Ca <sup>++</sup> concentration in leachate solutions for the 1315 leaching experiment. ....	36
Figure 18. Temporal change of total dissolved Si concentration. ....	36
Figure 19. Schematic diagram of the entire experimental column setup including flow control, sensors, and cartridge heater at the column center axis. ....	38
Figure 20. CT scan image showing the column cross section delineating the sampling radial zones . ....	38
Figure 21. XRD stacked spectra of bentonite sampled in region R3 (closer to the heater) for both heated (V1) and unheated (V2) column experiments. ....	40
Figure 22. XRD stacked spectra of bentonite sampled in region R2 (midpoint) for both heated (V1) and unheated (V2) column experiments. ....	40
Figure 23. XRD stacked spectra of bentonite sampled in region R1 (outer) for both heated (V1) and unheated (V2) column experiments . ....	41



## REVISION HISTORY

M4SF-21SN010301082

Rev0

## Acronym List

AD	Air-Dried
CTD	Closure Test Drift
DECOVALEX	DEvelopment of COupled models and their VALidation against EXperiments
DOC	Dissolved Organic Carbon
DOE	Department of Energy
DOE-NE	DOE Office of Nuclear Energy
DPC	Dual-Purpose Canisters
DSC	Differential Scanning Calorimetry
DTA	Differential Thermal Analysis
EBS	Engineered Barrier System
EDS	Energy Dispersive Spectroscopy
EDZ	Excavated Disturbed Zone
EG	Ethylene Glycol
EPA	Environmental Protection Agency
FEBEX-DP	Full-scale Engineering Barrier Experiments – Dismantling Project
GREET	Groundwater REcovery Experiment in Tunnel
GTS	Grimsel Test Site
H-C or HC	Hydro-Chemical
ICP-OES	Inductively Coupled Plasma Optical Emission Spectroscopy
ICP-MS	Inductively Coupled Plasma Mass Spectrometry
JAEA	Japan Atomic Energy Agency
MD	Molecular Dynamics
Na-MMT	Na-Montmorillonite or Sodium Montmorillonite
R&D	Research & Development
RH	Relative Humidity
RSA	Reactive Surface Area
SEM	Scanning Electron Microscopy
SF	Spent Fuel
SFWD	Spent Fuel and Waste Disposition
SNL	Sandia National Laboratories
TGA	Thermo-Gravimetric Analysis
THC	Thermal-Hydrological-Chemical
THMC	Thermal-Hydrological-Mechanical-Chemical
TST	Transition State Theory

TUL	Technical University of Liberec
URL	Underground Research Laboratory
XRD	X-ray Diffraction
XRF	X-ray Fluorescence

## I. Introduction

This interim report is an update of ongoing experimental and modeling work on bentonite material described in Jové Colón et al. (2019, 2020) from past international collaboration activities. As noted in Jové Colón et al. (2020), work on international repository science activities such as FEBEX-DP and DECOVALEX19 is either no longer continuing by the international partners. Nevertheless, research activities on the collected sample materials and field data are still ongoing. Descriptions of these underground research laboratory (URL) R&D activities are described elsewhere (Birkholzer et al. 2019; Jové Colón et al. 2020) but will be explained here when needed. The current reports recent reactive-transport modeling on the leaching of sedimentary rock.

Bentonite material obtained from the FEBEX-DP dismantling phase of heater #2 (see Fig. 1; Section II) is still used in current calorimetric studies to investigate hydration/dehydration phenomena of this material at elevated temperatures. The FEBEX-DP phase was performed during 2015 involving the careful retrieval of (FEBEX) bentonite barrier material samples from the remaining sections of the FEBEX “*in situ* test” at the Grimsel test site (GTS) URL, Switzerland, after 18+ years of heating (García-Siñeriz et al., 2016; Martinez et al., 2016). The disassembling activity involved sampling of the barrier bentonite, steel liner, sensors, embedded metallic components (e.g., metal coupons), and near-field sections with tracer components. Samples collected in section 49 experienced the hottest zones given its location close to the center of the (cylindrical) heater longitudinal axis. Jové Colón et al. (2019, 2020) describes the FEBEX-DP bentonite XRF compositional data along with XRD analyses, volumetric adsorption/desorption, and thermogravimetric analysis (TGA/DSC) with controlled hydration/dehydration cycles on bentonite samples collected as a function of distance from the gallery center or heater surface. Some of these experimental investigations are still ongoing for calorimetric and structural measurements conducted under variable temperature and relative humidity (RH) conditions. Information from calorimetric analyses (TGA/DSC) along with of recently obtained *in situ* XRD measurements on samples collected from the FEBEX-DP dismantling phase has been used with molecular dynamics (MD) simulation studies to evaluate montmorillonite hydration/dehydration behavior.

Jové Colón et al. (2020) describes results of the reactive transport modeling conducted as part of DECOVALEX-2019 Task C activity which involves collaboration with the GREET (Groundwater REcovery Experiment in Tunnel) at the Mizunami URL, Japan. Some of the goals of GREET were to conduct a facility-scale geochemical characterization study of short- and long-term effects of tunnel excavation activities, impacts on groundwater flow and transport, and influences on groundwater chemistry under ambient tunnel conditions (Iwatsuki et al., 2015). The hydrological and hydrochemical data obtained from these URL activities is then used in the development and evaluation of HC models to support post-closure safety and performance assessments of the repository environment. Jové Colón et al. (2019, 2020) and Birkholzer et al. (2019) describes 3D reactive transport (HC) modeling of the closure test drift (CTD) using the PFLOTRAN simulation tool focusing on shotcrete – ground water interactions of the cement liner in the water-filled tunnel. The collected field hydrological and hydrochemical monitoring data as a function of time is used to evaluate barrier material interactions effects on the flooded CTD water chemistry using a coupled-process model with heterogeneous permeability fields of the host rock surrounding the CTD. Jové Colón et al. (2020) provides the most recent results of the 3D reactive transport (HC) modeling of the CTD emphasizing on the importance of the

shotcrete liner thickness (or transport length scale) in the leaching process and related transport plus chemical reaction parameters to obtain the closest representation of the temporal changes in measured solute concentrations. This reactive transport simulation study greatly benefited from previous modeling efforts of idealized cement – clay rock interactions (Matteo et al. 2019). Given the importance of barrier material leaching on the chemistry of interacting aqueous phase solutions in the near- and far-field environments, an R&D collaboration as part of the international activities involves the 1D reactive transport modeling of leaching rock material under controlled laboratory conditions. This work is done in collaborations with the Engineered Barrier System (EBS) work package and involves the work of Dr. David Kosson's group at Vanderbilt University. Their work involves quantification of mass transport through laboratory leaching tests of well-characterized rock and cement samples. Solute concentrations from the leaching experiments are then used to evaluate parameters in both geochemical modeling of solution-mineral equilibria and reactive-transport simulations. A key aspect of this work is the comprehensive description of mass transport along interfaces for a system characterized for predominantly diffusive gradients. In this report, the current focus on modeling the leaching behavior of a marl rock monolith from sedimentary formations in the northern Negev, Israel (Matteo et al. 2020). The leaching test was conducted using the EPA method 1315 (U.S. EPA, 2017) to quantify mass transfer rates under saturated conditions. Details of these and other leaching tests on cement and monolith rock samples are described by Matteo et al. (2020).

The main goals of this report update for each of the international activities are:

- FEBEX-DP:
  - (Section III) Provide additional thermal analysis (DSC) data with controlled hydration/dehydration cycles on FEBEX-DP bentonite samples at temperatures of 85°C and 150°C. Only data for the dehydration steps is given in this report. In addition, present data of *in situ* XRD analyses under controlled dew point of ~58°C at a temperature of 85°C. Bentonite hydration/dehydration state controls swelling and shrinkage phenomena in bentonite.
  - (Section IV) Describe molecular dynamics (MD) simulation of Na-Montmorillonite (Na-MMT) dehydration focusing on water transport at the smectite interlayer. This modeling effort was motivated by the TGA/DSC, water adsorption isotherm experiments, and more recently *in situ* XRD analyses on FEBEX-DP bentonite samples to evaluate mechanism of water transport at the molecular level.
- PFLOTRAN Simulation of Marl Leaching:
  - (Section V) Describe 1D reactive-transport simulations with PFLOTRAN on a marl rock monolith. Mineralogic characterization, rock properties, and solute concentration vs. time data from leaching experiment were used to constrain transport and mineral dissolution rate parameters in the reactive-transport model.
- HotBent Heated Column Experiment:
  - (Section VI) Provide preliminary XRD data on treated bentonite material collected after shutdown of the laboratory-scale HotBent heated column experiment. This is part of the large scale HotBent heater test field experiment at the Grimsel site.

## II. FEBEX-DP

The post-closure period will experience high thermal loads that can drive fluid transport and barrier alteration in a variably saturated near-field environment. As a result enhanced interactions with fluids can induce phase transformation phenomena, and other potential mineralogical changes in bentonite. Jové Colón et al. (2016) describes the 2D-3D characterization of microcracks in bentonite in a FEBEX-DP shotcrete-bentonite overcore stressing the importance of desiccation/shrinkage processes in bentonite and the nature of pores/voids in shotcrete. Engineered barrier alteration has been assessed by reactive-transport models and geochemical modeling of mineral dissolution and precipitation (Marty et al., 2015; Wilson et al., 2015; Xie et al., 2015). An example is Fe-bentonite interactions which leading to mineral phase changes that could impact swelling capacity in bentonite through alteration to a non-swelling Fe-bearing phase. Also, cation exchange in the bentonite clay could also be impacted through temperature-induced drying and wetting causing variations in the cation exchange capacity (CEC) (Muurinen, 2011). Cation exchange experiments reported by Villar et al. (2017) show that FEBEX-DP bentonite samples collected from sections closest to the heater exhibit higher concentrations of Mg and Ca and low concentrations of exchangeable Na. Further, aqueous extracts for bentonite samples collected in sections close to the heater exhibited higher aqueous concentrations of Mg, Ca, Na, and Cl relative to those sampled farther away from the heater (Villar et al., 2017). These changes in the observed aqueous concentration from these tests suggest that bentonites close to the heater were affected by thermal loads therefore inducing changes in the smectite clay phase and potentially their subsequent interactions with fluids. Fig. 3 shows the radial locations of samples collected in Section 49 considered in this study. Section III describes further TGA/DSC analyses to FEBEX-DP bentonite samples at elevated temperatures under controlled moisture conditions. Motivated by the thermal studies, MD simulations of montmorillonite dehydration under certain conditions were conducted to describe this process at the molecular scale. These studies are discussed in Section IV.

FEBEX bentonite is composed of ~93% smectite with 2% quartz, 3% plagioclase, and about 2% cristobalite plus minor accessory phases such as calcite and K-feldspar (Huertas et al., 2000; Missana and García-Gutiérrez, 2007). The extent of the corroded region from the heater steel mesh support surface into the bentonite is rather limited which might explain the relatively low level of Fe alteration into the bentonite, particularly in the hotter zones of the heater.

The XRD data reported in Jové Colón et al. (2018) has been evaluated and compared between samples close to and far from the heater surface and that for unheated FEBEX bentonite. As described in Jové Colón et al. (2018), a salient feature revealed by XRF compositional analyses is the increase in Mg content with decreasing distance from the heater or towards the heater surface (~50 cm from the gallery center). An explanation for the Mg enrichment close to the heater surface is still under investigation. Potential mechanisms to be considered are (1) enhanced cation exchange of Mg from pore solution into smectite and (2) enhancement of Mg content already in smectite through removal of other readily exchangeable cations such as Na<sup>+</sup>.

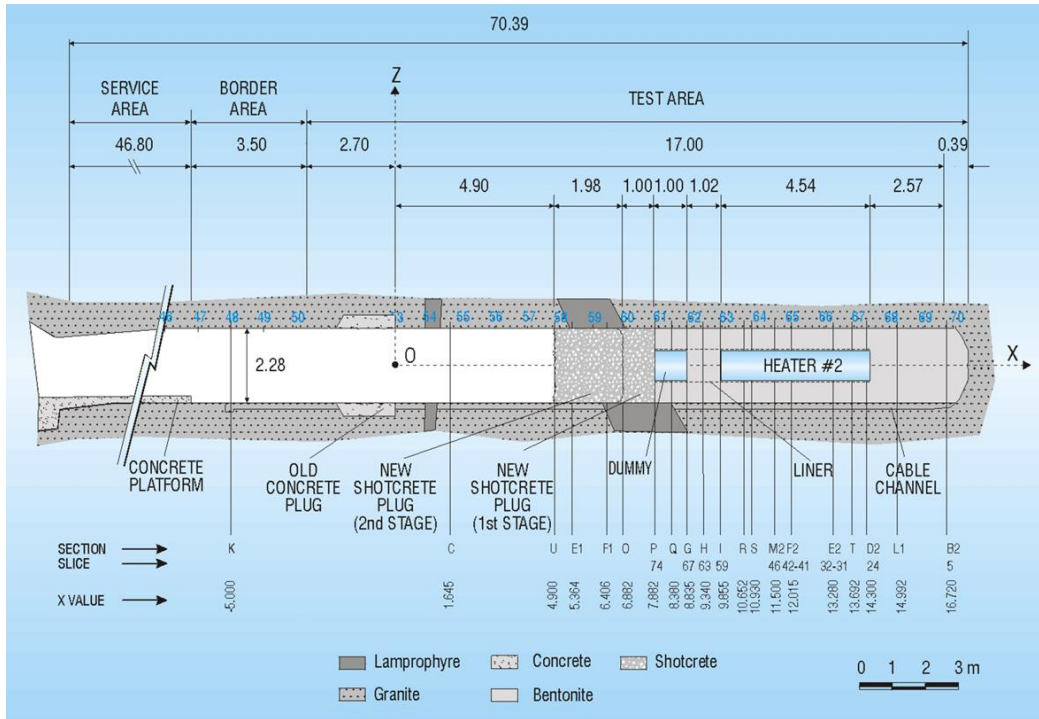


Figure 1. Schematic layout of the FEBEX “in-situ” field test after the first partial dismantling showing the configuration of heater #2 at the GTS URL (García-Siñeriz et al., 2016).

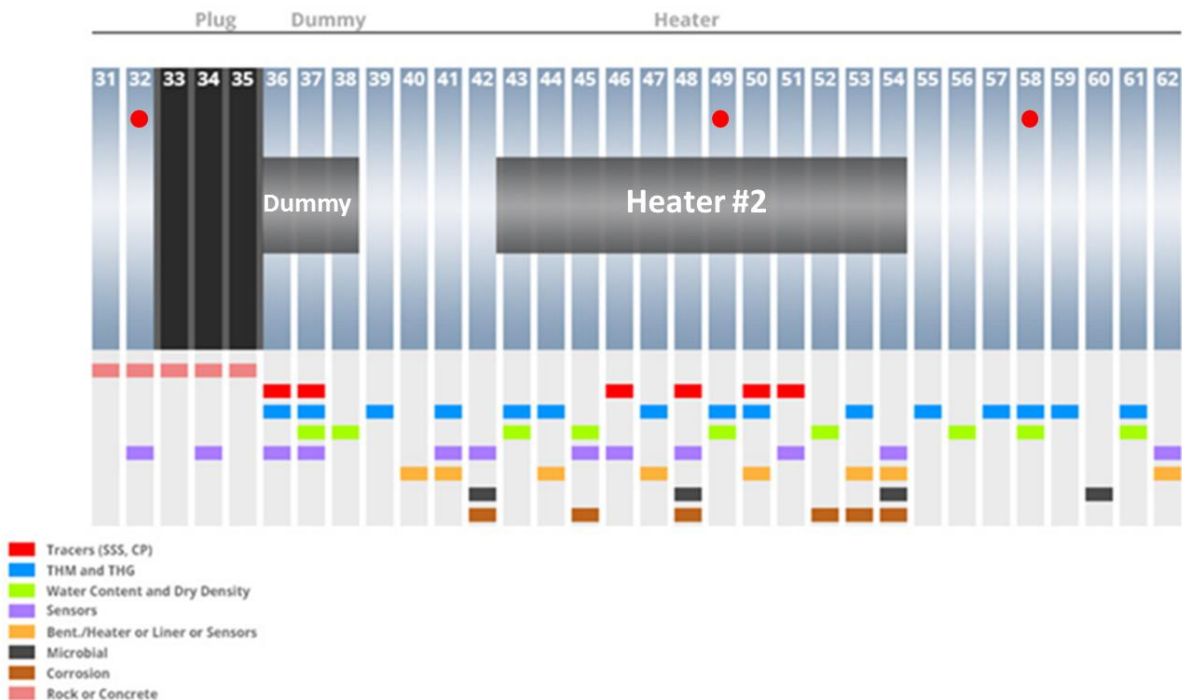


Figure 2. Schematic configuration of sampling zones (indicated by vertical light blue bars) for the FEBEX-DP project. Filled red circles indicate zones for samples obtained by Sandia National Laboratories (SNL). Source: FEBEX-DP website (members area): <http://www.grimsel.com/gts-phase-vi/febex-dp/febex-dp-introduction>.

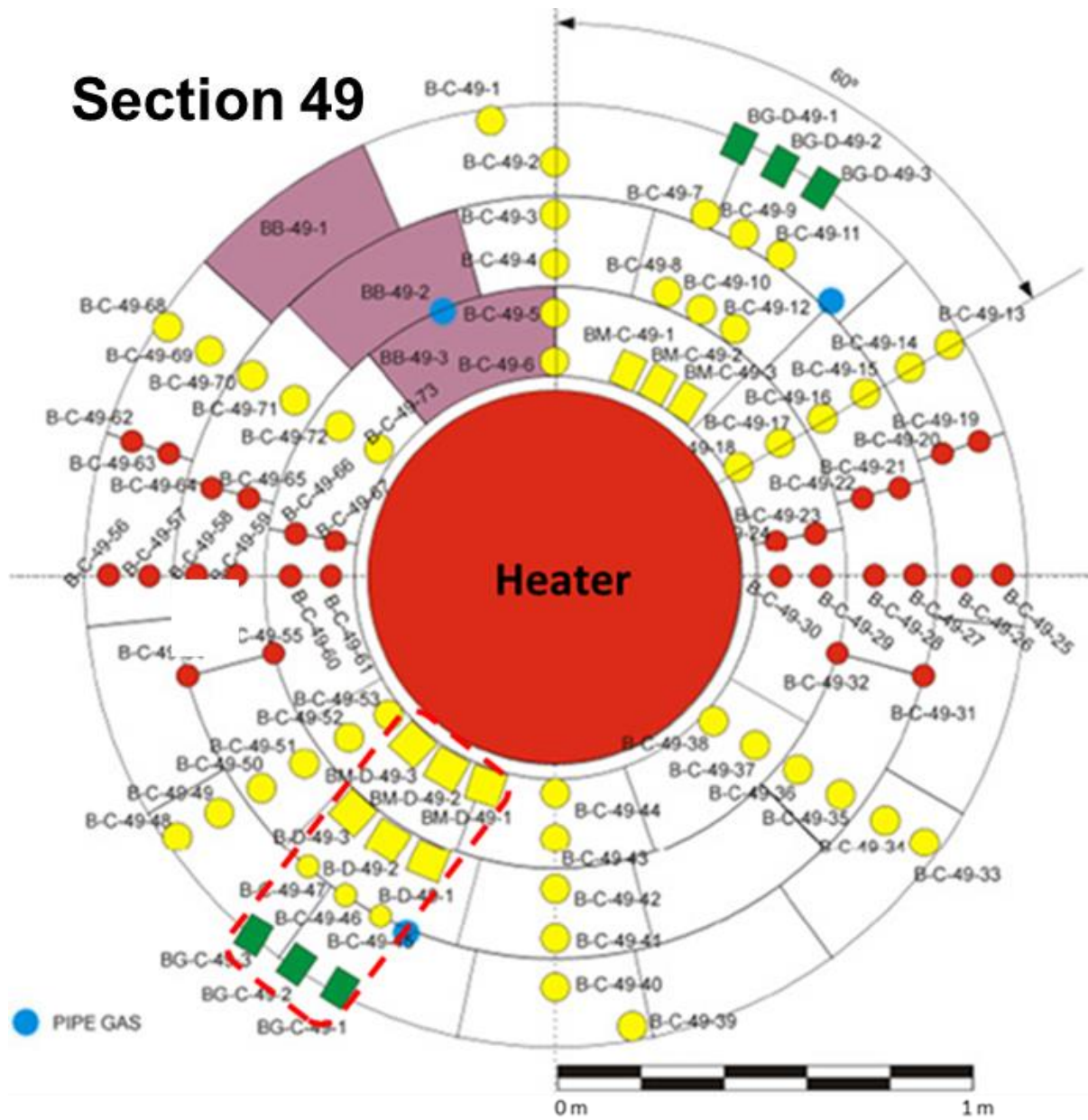


Figure 3. Schematic diagram of sampling locations for the FEBEX-DP dismantling of section 49. See Fig. 2 for section location relative to the heater zone. The red-dashed line delineates the locations of samples analyzed with XRD and XRF (diagram source: FEBEX-DP website (members area): <http://www.grimsel.com/gts-phase-vi/febex-dp/febex-dp-introduction>).



### III. Thermal (TGA/DSC) Analyses

Water adsorption/desorption behavior in expansive clay is key to this material swelling phenomena but also to water transport during hydration/dehydration processes. Thermal loads in deep geological nuclear waste repositories control RH conditions in the disposal galleries where bentonite is used as backfill barrier material. Therefore, chemo-mechanical responses and mechanisms of bentonite hydration/dehydration to changes in RH and temperature are crucial to the EBS performance. Cyclical TGA/DSC analyses under controlled RH and temperature provides important information on the kinetics of expansive clay hydration/dehydration and also provides insights on the hysteretic behavior of this process.

It should be noted that the COVID-19 situation impacted some of the laboratory activities due to laboratory shutdowns or restricted access with limited personnel under very strict working conditions. Still, some of the planned TGS/DSC experiments and *in situ* XRD analyses were conducted to temperatures of 85°C (TGA/DSC and *in situ* XRD) and 150°C (TGA/DSC only). This section of the report focuses on providing the data obtained so far but the evaluation of these results is still ongoing. It should also be noted that the *in situ* XRD setup is no longer operational. However, there are plans to continue this activity on bentonite when a functional XRD equipment becomes available.

Jové Colón et al. (2019, 2020) provides TGA/DSC analysis and water adsorption/desorption data for bentonite samples close and far from the heater surface. contained in Appendix A of Jové Colón et al. (2020). These analyses were conducted Section 49 bentonite samples using a Netzsch STA 449 F3 Jupiter with MHG humidity generator. The analyzed samples are the unheated FEBEX bentonite, BG-C-49-1, BG-C-49-3, B-C-49-7, B-C-49-8, B-C-49-11, B-C-49-12, BM-D-49-3, BM-D-49-1,2,3. Thermal analysis (thermogravimetric analysis, TGA, and Differential Scanning Calorimetry, DSC) was conducted using an STA 449 F3 Jupiter (Netzsch, Germany) with MHG humidity generator (ProUmid, Germany). The bentonite sample (ca. 20 mg) was placed in a platinum crucible and loaded into the thermal analyzer. Since the hydration state of the material as-received was not defined, it was subjected to a drying process prior to humidity cycling. Under a constant flow of dry nitrogen (200 ml/min) the specimen was heated to 150°C at 10°C/min and held for 30 minutes, then cooled to 85°C and held for about 60 minutes to ensure a consistent (dry) starting point for analysis. Bentonite hydration was carried out under a flow of 200 ml/min humid nitrogen (dewpoint 58°C); and dehydration occurred under a 200 ml/min flow of dry nitrogen. After each hydration-dehydration cycle at 85 C, the specimen was dried by heating to 150°C under 200 ml/min dry N<sub>2</sub> and holding for 30-60 minutes before cooling to 85°C and beginning the next cycle. For the tests at a hydration-dehydration temperature of 150°C, the procedure was the same as described above, but omitting the additional drying steps between each cycle.

For the cyclical TGA/DSC analyses under controlled RH and a temperature of 60°C, bentonite samples were initially exposed to dry N<sub>2</sub> heated (10°C/min) to 100°C holding this temperature for 30 minutes. Still under dry N<sub>2</sub>, the temperature was increased (10°C/min) to 150°C for another 30 minutes. Subsequently, the temperature was decreased to 60°C for 60 minutes to the expose the bentonite to a succession of dry and humid cycles (60 % RH in the generator; 50% RH close to the sample) by flowing water-wet and dry N<sub>2</sub> atmospheres to hydrate and dehydrate the samples. Cyclical hydration/dehydration provides key information about the adsorption/desorption rates of water, quantity of water adsorbed, and energetics of hydration/dehydration reaction. Villar et al. (2017) performed TGA/DSC on FEBEX-DP

bentonite from other sampled sections. Overall, the TGA/DSC profile up to high temperatures of Villar et al. (2017) and that obtained for bulk FEBEX bentonites from Section 49 are generally similar as shown in Jové Colón et al. (2018). To the knowledge of the authors, with exception of the results reported in Jové Colón et al. (2019, 2020), no cyclical hydration/dehydration TGA/DSC study on bentonite has been conducted under controlled RH and temperature conditions. The advantage of this approach is that allows for accurate kinetic studies of water adsorption/desorption cycles for given interval durations at constant RH under controlled isothermal conditions. It also allows for characterizing the effects of thermal treatment on bentonite water adsorption/desorption.

Fig. 4a (taken from Jové Colón et al., 2020) shows a representative temporal TGA/DSC profile of water adsorption/desorption cycles at 60°C as a function of time (minutes) for the less than 2  $\mu\text{m}$  sample. The green line in Fig. 4a this graph depicts the mass of the sample as it responds to changing RH during water adsorption/desorption cycles. Panels b and c of Fig. 4 depict the desorption steps only, represented by TGA and differential TGA (or DTA) in panel b, and DSC in panel c. Notice that the x-axes in these panels refers to dehydration time. The data in these plots show that the dehydration behavior is clearly a function of the duration of hydration that precedes it. Short duration hydration steps (i.e., less than two hours; curves A-D in Fig. 4) result in a dehydration process that is almost complete relative to the “dry” baseline of these cycles within a time span of approximately 45 minutes after switching back to dry gas. This is represented by a single dehydration peak in both DTA and DSC plots. As the duration of the hydration step increases beyond two hours (curves E-G in Fig. 4), however, the subsequent dehydration takes a more complex form, with a changing slope in the TGA curve and clearly shown as negative peaks in the DTA plots. Note that these show up as endotherms in the DSC plots and do not begin at the onset of the bentonite dehydration, but some time thereafter.

Notice that the DTA and DSC traces are essentially mirror images of each other, since any loss of mass of the sample (DTA) is accompanied by a heat flow signal that is proportional (DSC). Fig. 5 present similar data as in Fig. 4 for the <75  $\mu\text{m}$  bentonite samples at 60°C but for the dehydration steps only. Similar behavior for these two larger grain sizes was observed when compared to the 2  $\mu\text{m}$  sample.

Figs. 4 and 5 show a trend with increasing hydration time periods, in particular with regards to endothermic peaks in the DSC thermograms (Figs. 4c and 5b). For FY21, we planned to conduct thermal analyses at higher temperatures to further study this behavior under such conditions. Fig. 6 shows DSC thermograms at 85°C and 150°C (Figs. 6a and 6b, respectively) at a dew point of ~58°C. TGA data (not shown) was also obtained as part of these thermal analyses. The trend observed in the DSC thermograms in Fig. 6 are somewhat similar to those at 60°C up to a hydration time period of 120 minutes. However, at hydration time periods of 120 minutes or more the trend in the endothermic peaks is no longer defined by the data. There are other features in the endothermic peaks that need further evaluation and those efforts are ongoing.

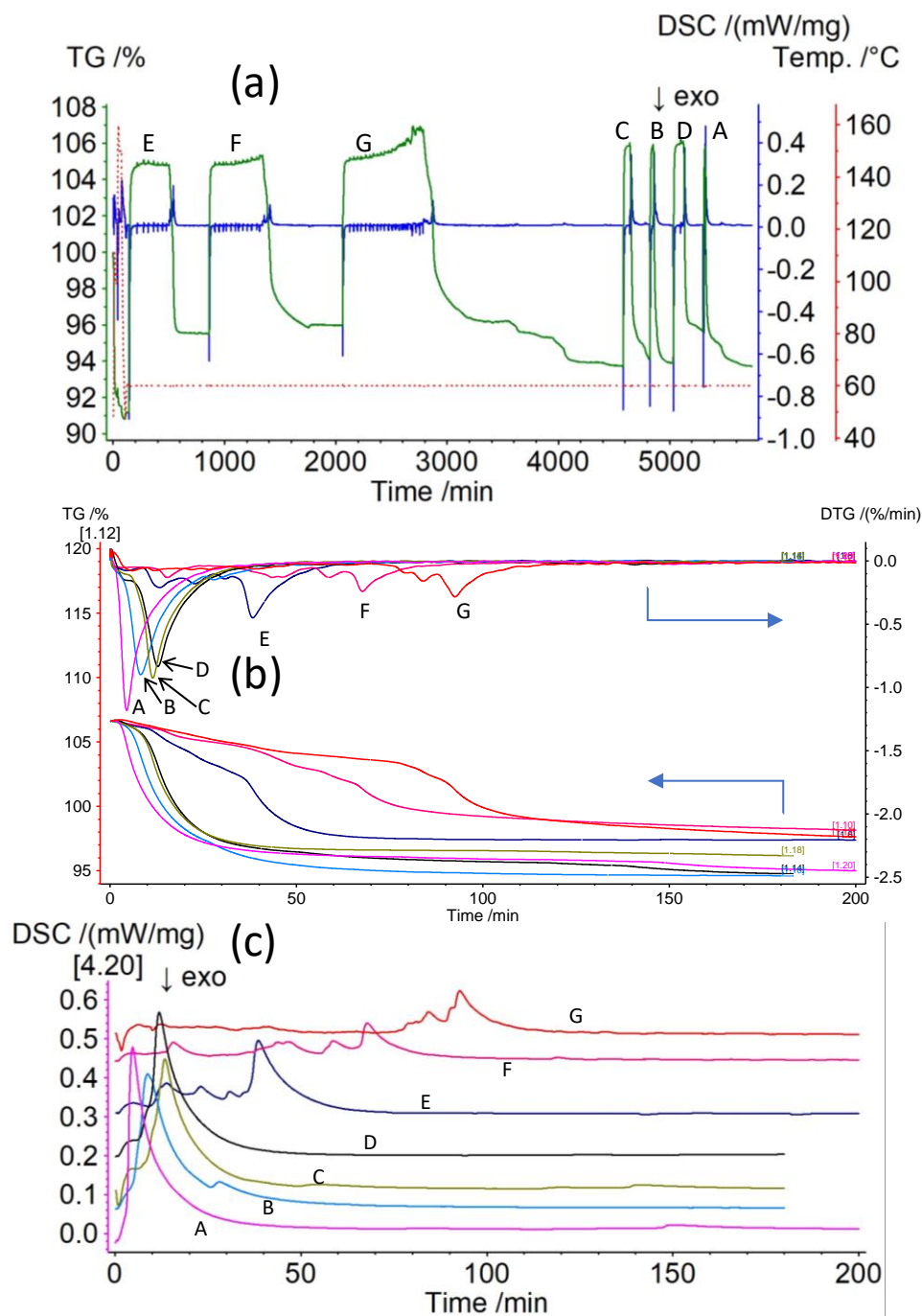


Figure 4. TGA, DTA, and DSC curves as a function of time for water adsorption/desorption cycles at 60°C for the <2 μm bentonite sample. (a) The green curve represents the thermogravimetric analysis (left y-axis). The blue curve stands for the DSC analysis (right y-axis). The red dotted line signifies the temperature (2<sup>nd</sup> right y-axis). The period of hydration was varied for each cycle, as depicted by the curve labels; A = 15 min, B = 30 min, C = 1 hour, D = 1.5 hours, E = 6 hours, F = 8 hours, and G = 12 hours. (b) TGA (lower) and DTA (upper) curves for the dehydration steps only, plotted against dehydration time. Curve labels identical to panel (a). (c) DSC measurements as a function of elapsed time for the dehydration steps; curves have been offset arbitrarily on the y-axis for clarity. (Jové Colón et al., 2020)

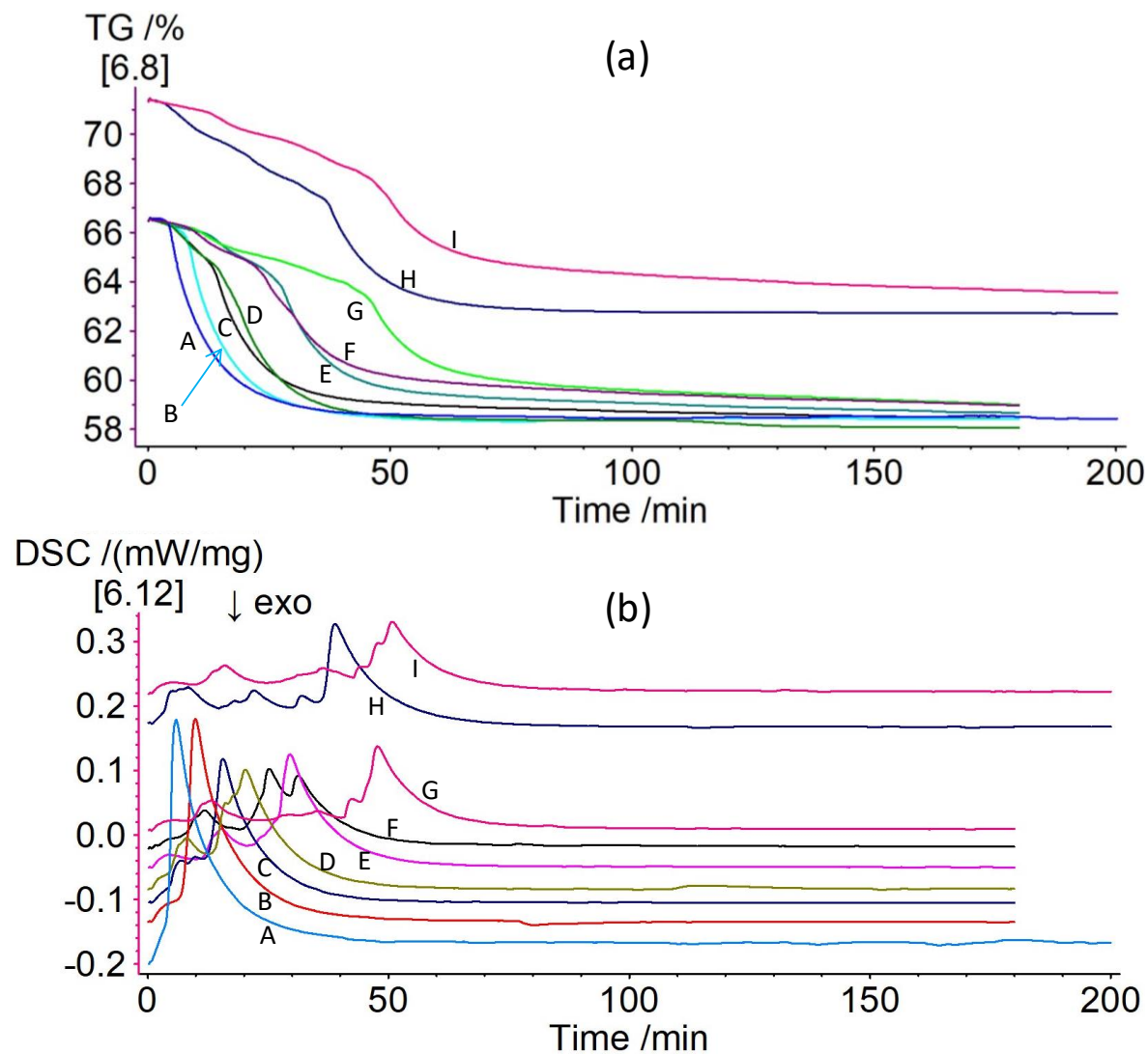


Figure 5. TGA and DSC curves as a function of time for water adsorption/desorption cycles at 60°C for the <75 μm bentonite sample. (a) TGA curves for the dehydration steps only, plotted against dehydration time. The period of hydration was varied for each cycle, as depicted by the curve labels; A = 15 min, B = 30 min, C = 1 hour, D = 1.5 hours, E = 2 hours, F = 3 hours, G = 4 hours, H = 6 hours, and I = 8 hours. (b) DSC measurements as a function of elapsed time for the dehydration steps; curves have been offset arbitrarily on the y-axis for clarity. Curve labels identical to panel (a).

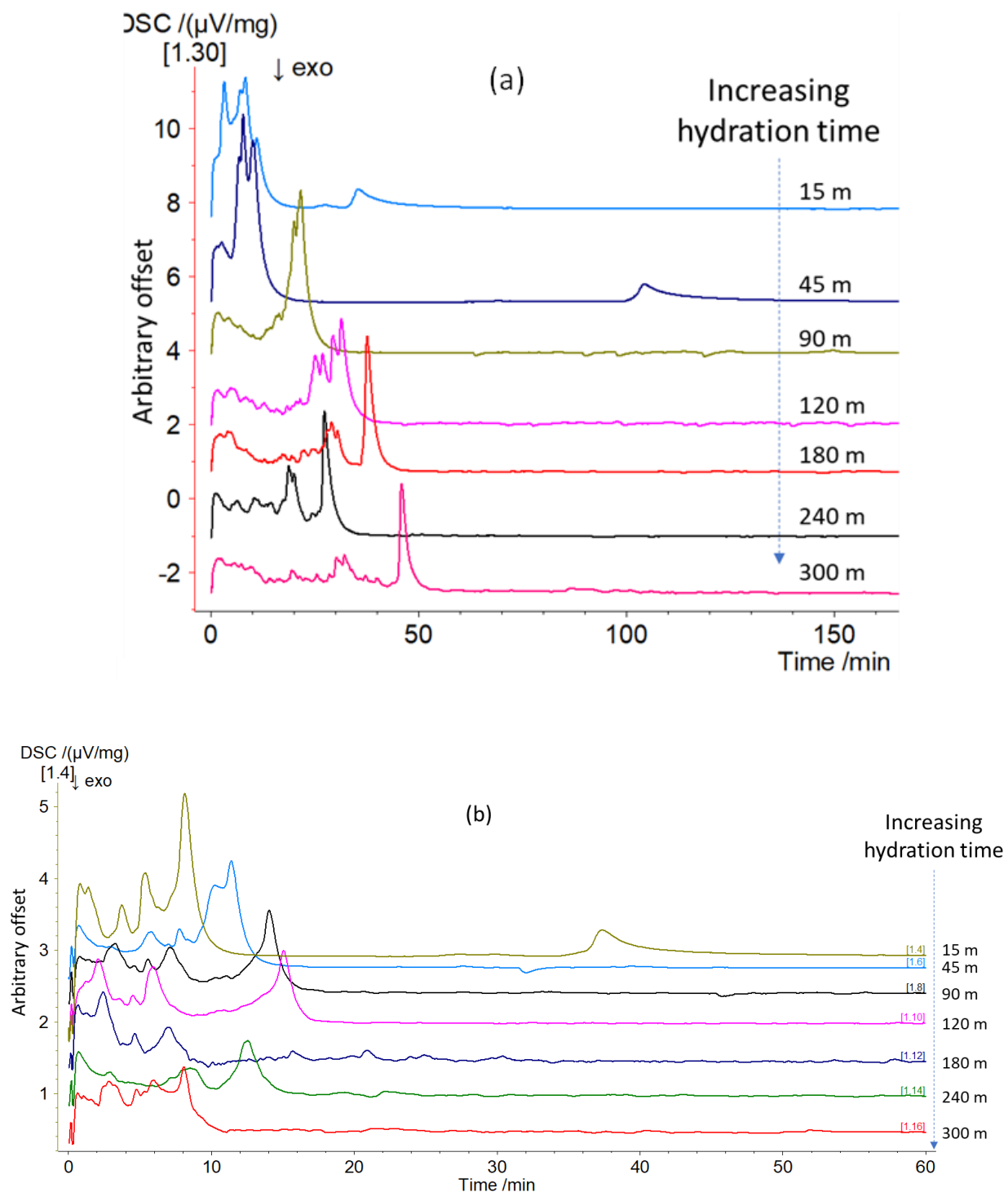


Figure 6. DSC curves as a function of time for the  $<2 \mu\text{m}$  bentonite sample for the dehydration steps at (a)  $85^\circ\text{C}$  and (b)  $150^\circ\text{C}$ . The moisture environment was set to a dew point of  $\sim 58^\circ\text{C}$  at both temperatures. The period of hydration was varied for each cycle, as depicted by the curve labels from 15 to 300 minutes. The curves have been offset arbitrarily on the y-axis for clarity.

*In situ* XRD analyses were conducted at 85°C at a dew point of ~58°C. A few spectra was collected at 150°C under dry He conditions during heating. This analysis was performed using a Scintag Pad-X diffractometer equipped with a Buehler heated reaction chamber, and home-built gas and vapor delivery system. A specimen of bentonite powder was sprinkled onto a silicon wafer to make a flat bed of powder < 1 mm thick. This was placed in the reaction chamber within the diffractometer and a constant flow of helium gas (100 ml/min) was flowed through the reaction chamber. The reaction chamber was then heated to 85°C and held at that temperature for the entire experiment. In order to hydrate the sample, the helium was passed through a sparger immersed in deionized water maintained at 50 +/-5 °C. Once the hydration period (ca. 5 hours) was complete, the water sparger was bypassed. All lines between the sparger and the reaction chamber were traced with heat tape to minimize condensation of water in the lines.

Fig. 7 shows the *in situ* XRD data at 85°C and 150°C (heating) illustrating the changes in the 001 peak (7-10° 2-theta) with variations in moisture conditions. Notice the broadening of the 001 peak in the periods of hydration (humid He) along with its shift towards lower 2-theta, as expected, for a more hydrated state (larger 001 d-spacing). As the system is driven towards drying conditions, the opposite is observed where the 001 peak becomes sharper, shifting towards higher 2-theta (smaller 001 d-spacing). Fig. 8 depicts the variation of the 001 d-spacing with time during hydration/dehydration at a temperature of 85°C. The 001 d-spacing data looks similar to that collected at 60°C where upon switching to dry He, there is a relatively slow change before a fast and sharp drop is observed followed by a slow decaying change with continuous dehydration. This is the last set of data collected prior to equipment failure.

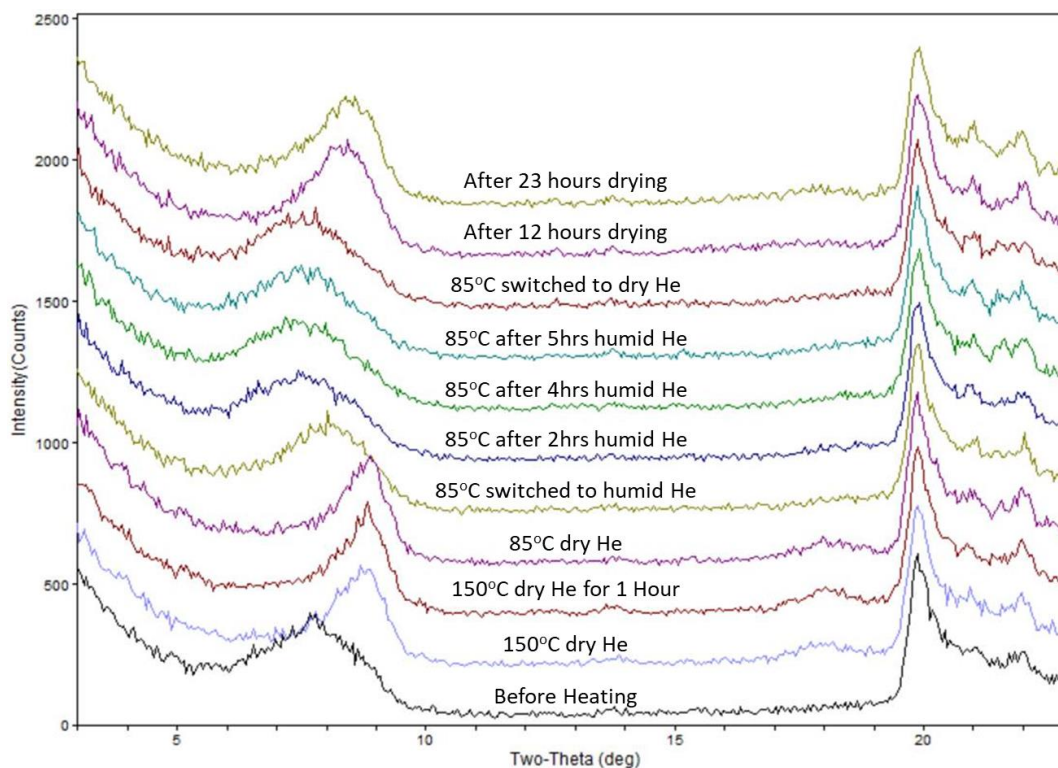


Figure 7. *In situ* XRD spectra collected at temperatures of 85°C and 150°C, and at a dew point of ~58°C. The stacked curves have been offset arbitrarily on the y-axis for clarity.

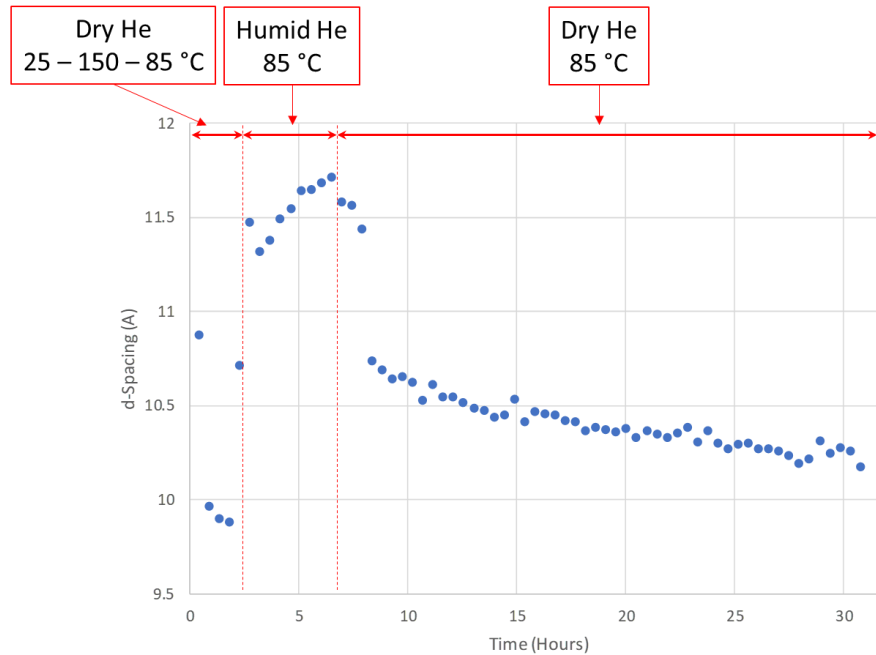


Figure 8. *In situ* XRD 001 d-spacing data for clay hydration/dehydration states collected at temperatures of 85°C and a dew point of ~58°C.

Analysis of these data is currently ongoing and is still work in progress. As before, these observations will be used with molecular dynamics (MD) simulation (Section V) to describe the mechanisms of water behavior in the smectite interlayer during evaporation. Further work is planned to conduct more cyclical TGA/DSC to further evaluate the effect of hydration time durations at higher temperatures. Similarly, there are also plans for more XRD studies under controlled RH and temperature to complement the cyclical TGA/DSC experiments when the equipment becomes available. An important aspect of these thermal studies is to assess the impact of temperature on bentonite swelling and water uptake given the anticipated high thermal loads from large canisters (e.g., dual purpose canisters or DPC's) on the surrounding bentonite barrier.

#### IV. Transport-mechanical-chemical coupling effect during clay dehydration controlled by coordination number of interlayer ions

Expansive clays [e.g., montmorillonite (MMT)] are phyllosilicate minerals that can adsorb a large quantity of water into interlayers resulting in very complex chemo-mechanical behavior in many environmental, geological (energy resources), and industrial systems – including the engineered barrier system (EBS) in deep-geological nuclear waste repositories (Busch et al., 2008; Gates et al., 2009; Amato, 2013; Arthur and Cole, 2014; Jové Colón et al., 2014). Understanding thermal-hydraulic-mechanical-chemical (THMC) coupling effects during clay swelling/shrinking is key to the behavior of backfill bentonite material and water transport in the near-field environment. The accuracy of a THMC model representation depends on the fundamental understanding of the link among surface charge, interlayer ion, water structure and dynamics, temperature, pressure, relative humidity (RH), d-spacing, and swelling pressure (Teich-McGoldrick et al. 2015; Marty et al. 2020). Such understanding can be extracted from laboratory experiments investigating a d-spacing of a clay sample using X-ray diffraction (XRD) technique in a controlled RH chamber (Morodome S and Kawamura, 2009; Ferrage et al., 2010;

Tamura et al., 2000; Yamada et al., 1994). A swelling curve (e.g., d-spacing vs. RH) provides a macroscopic mechanical-chemical relation that a d-spacing abruptly increases (i.e., stepwise swelling mechanism) with increasing number of water layers from zero (0W) to one (1W), two (2W) or three (3W) in an interlayer when the RH increases (Clark et al., 1937). Clays with different surface charge, charge location, and interlayer ion were intensively studied (Sun et al., 2015; Vinci et al., 2020; Liu et al., 2008) that provide relatively advanced knowledge about the macroscopic properties of expansive clays. However, experiments often probe equilibrium hydration states in an averaged manner, and have not been able to directly capture the microscopic features in a rapid swelling/shrinking process (Moyné and Murad, 2002).

Simulation techniques such as reactive transport modeling employ undeformed mesh in a finite element analysis that makes it difficult to simulate the deformation of materials and barely provide microscopic insights into the properties of a clay system. In contrast, inherent to its molecular description, molecular simulations provide a feasible approach to model the deformation of materials coupled with molecular behaviors of simulated systems (Ho et al., 2018). Unfortunately, most molecular dynamics simulations studying clay hydration/dehydration focus on structural and dynamics properties of water/ion in the clay interlayers at a certain hydration state (Holmboe et al., 2014; Ngouana et al., 2014; Rotenberg et al., 2007; Greathouse et al., 2016; Chang et al., 1995; Morrow et al., 2013). The deformation of materials from one hydration state to another, coupling with chemical alteration and water transport in the interlayer remains not well understood (Ho et al. 2019a; Whittaker et al., 2019).

Furthermore, our knowledge regarding the thermodynamic state (e.g., gas, liquid, ice-like) and transport mechanism of water molecules in the clay interlayers and its effect on swelling/shrinking is unfulfilled, compared with the knowledge acquired for other layered materials such as graphene and graphene oxide. For example, in graphene oxide interlayers, water transport is superfast in hydrophobic (graphene) regions and hindered in hydrophilic oxidized regions (Nair et al., 2012). A montmorillonite surface can have hydrophobic sites associating with siloxane groups, and hydrophilic sites associating with metal substitution in the octahedral and/or tetrahedral sheets. The abundance of these sites depends on the number of metal substitutions (i.e., surface charge density). The effect of these sites on water transport and deformation of clay has not yet been unveiled. In addition, in graphene interlayers water can flow fast due to the slip boundary condition, and such fast water flow can be modeled using a modified Hagen-Poiseuille (HP) equation, meaning that water is a Newtonian liquid (i.e., viscosity remains constant regardless of the flow rate) (Radha et al, 2016). In general, viscosity of a nano-confined fluid is different from that of bulk fluid (Ho et al. 2019b; Chen et al., 2008; Neek-Amal et al., 2016; Ye et al., 2011; Babu et al., 2011; Ortiz-Young et al. 2013). Our previous work suggested that water in the 2W state might be a Newtonian fluid with a viscosity ~3-5 times higher than bulk viscosity, and that water can flow fast in the interlayer due to a large suction pressure (~800 MPa) induced by evaporation (Ho et al., 2020). Our previous work also suggested that water transport in the early stage of the dehydration of clay can be a HP flow, followed by a slow diffusion process. Neither simulations nor experiments have been able to explore the correlation between the flow regime change with the modification of the hydration structure and chemistry of interlayer ions. We here combine molecular dynamics (MD) simulations, thermogravimetric analysis (TGA), differential scanning calorimetry (DSC), and XRD experiments to probe the atomic resolution dynamics of the dehydration process. Our result provides a molecular picture of the coupling nature of water transport mechanism and pathway, and the collapse of clay hydrated structure.



## Method

Fig. 9 represents a MD simulations system we used to study the water transport mechanism in the interlayer and structural transformation of hydrated Na-MMT during the dehydration process. The Na-MMT particle, with 10 interlayers in total, has 2 edges facing the vacuum. The method to build the Na-MMT particle can be found in our previous work (Ho et al., 2019a). Briefly, from a pyrophyllite structure we create a pyrophyllite particle with edges and then substitute octahedral Al atoms by Mg atoms to obtain Mg:Al ratio of 0.75:3.25.  $\text{Na}^+$  ions are added to the interlayers to balance the negative charges, a result of metal substitution. Water molecules are also added to obtain the 1W or 2W hydration state. The 1W or 2W hydrated Na-MMT particle is first equilibrated in an NPT (constant number of particles, pressure (coupled in the x direction), and temperature) simulation, followed by a dehydration simulation. During the dehydration simulations water molecules that move to the vacuum space (i.e., between the dash line and boundary of the simulation box) are removed at a constant rate of 5 molecules per picosecond (i.e., 5 w/ps) (Ho et al., 2016). In other words, as dehydration progresses, water molecules move from the center of the particle to the edge and are removed. Note that the removal rate used in MD is much higher than the evaporation rate at a free surface. For example, at 20% RH, 24.3°C, and 1.5 m/s of air velocity, the evaporation rate from a vessel of diameter 9.3 cm is  $\sim 1$  mg/min.cm<sup>2</sup> (Hisatake et al., 1993), corresponding to  $5.19 \times 10^{-7}$  w/ps for our simulated system. Because of the limited computational resource and the small MD system size, the removal rate simulated is a reasonable choice.

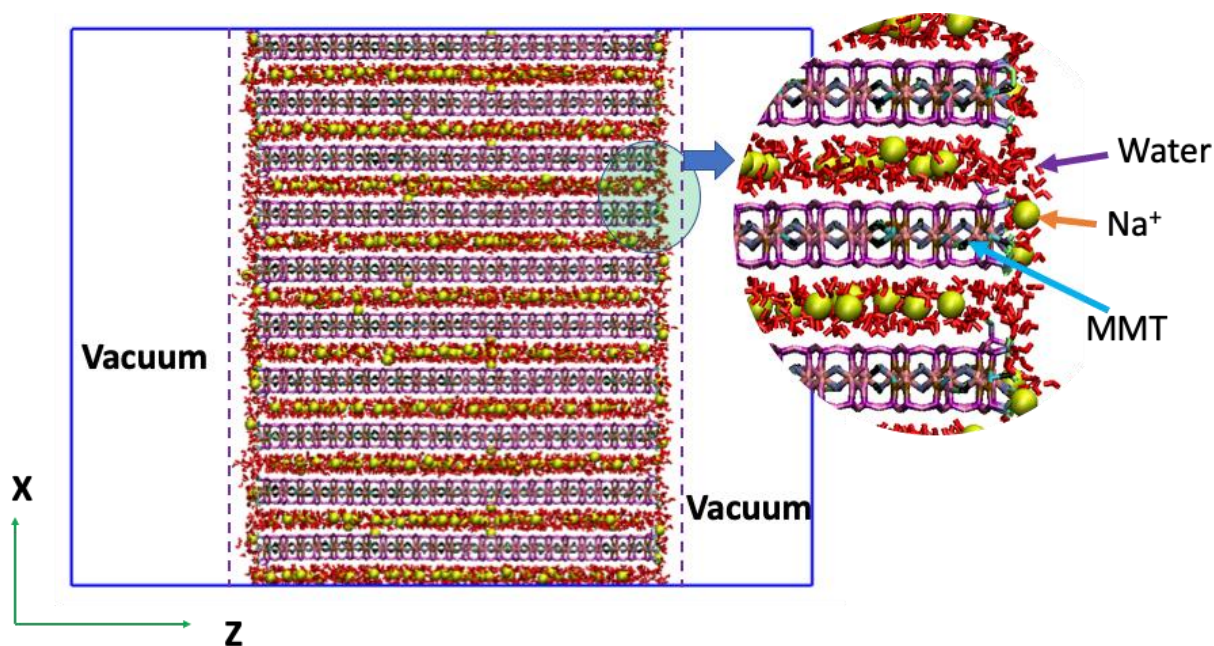


Figure 9. Simulation system used to study the dehydration process of Na-MMT. The simulation box size is  $150 \times 31.06 \times 200 \text{ \AA}^3$ . When applying periodic boundary conditions for all directions, the Na-MMT particle becomes infinite in the x and y directions and finite in the z direction.

There are two processes determining the dehydration: water transport through the interlayer, and water removal (i.e., evaporation) from the edge. If the maximum possible water transport rate is equal to or higher than the evaporation rate then the number of water molecules removed from the system equals the evaporation rate. If the maximum water transport rate is smaller than the evaporation rate then the number of water molecules removed depends on the water transport

rate. During the dehydration simulation, the simulation box can shrink in the x direction under the influence of 1 atm pressure. This unique simulation setup allows us to simultaneously study the water transport, the collapse of the clay particle, and chemical changes in the interlayer. This simulation system is analogous to our experimental setup: a stream of dry N<sub>2</sub> at atmospheric pressure was passed over the hydrated sample for dehydration. The sample was hydrated at 60°C and 50% RH. The mass evolution, heat change, and d-spacing of the sample are monitored in-situ as a function of time using TGA/DSC, and XRD techniques. These methods are described in the previous section.

The Na-MMT particle is simulated by the ClayFF force field (Cygan et al., 2004) with additional Si-O-H and Al-O-H angle terms describing edge hydroxyl groups (Pouvreau et al., 2017; 2019). CLAYFF force field is parameterized with the flexible SPC water model (Teleman et al., 1987) and the Smith and Dang (1994) Na<sup>+</sup> ions model. The pairwise Lennard-Jones (LJ) potential energy is expressed as:

$V_{LJ} = 4\epsilon \left[ \left( \frac{\sigma}{r} \right)^{12} - \left( \frac{\sigma}{r} \right)^6 \right]$ , where  $r$  is the distance between two atoms,  $\epsilon$  and  $\sigma$  are the depth of the potential energy well and the distance at which the LJ potential is zero, respectively. LJ interactions among atoms are calculated using the Lorentz-Berthelot mixing rules  $\epsilon_{ij} = \sqrt{\epsilon_{ii}\epsilon_{jj}}$  and  $\sigma_{ij} = (\sigma_{ii} + \sigma_{jj})/2$ . Short range interactions are calculated using a cut-off distance of 10 Å. Long range electrostatic interactions are calculated using the particle-particle-particle-mesh (PPPM) solver (Hockney and Eastwood, 1988). The simulations are conducted at 300 K or 330 K using the Nose-Hoover thermostat (Nosé et al., 1984; Martyna et al., 1994). The LAMMPS package (Plimpton, 1995) is used for all molecular dynamics (MD) simulations with a timestep of 1.0 fs.

## Results

In Fig. 10 we report the mass loss (i.e., number of water molecules removed from the simulation system) as a function of simulation time during the dehydration simulation. We observe a two-stage dehydration process. At the beginning of the simulation (point A in the top left panel of Fig. 10), there are two hydration layers in an interlayer (snapshot A). As the dehydration progresses, the mass loss linearly increases from point A to point B (first stage). The snapshot B indicates that at point B, there is one hydration layer in an interlayer (1W). The linear relationship is an indication that water movement through the nanochannel is faster than the water removal rate imposed, and can be modeled as advection flow (Ho et al. 2020). Further dehydration increases the mass loss nonlinearly (second stage). The nonlinear correlation indicates that the water transport rate through the interlayer is smaller than the evaporation rate, suggesting a diffusion mechanism for water transport in the second stage of the dehydration process (Ho et al. 2020). At point C, there are few water molecules in an interlayer (snapshot C).

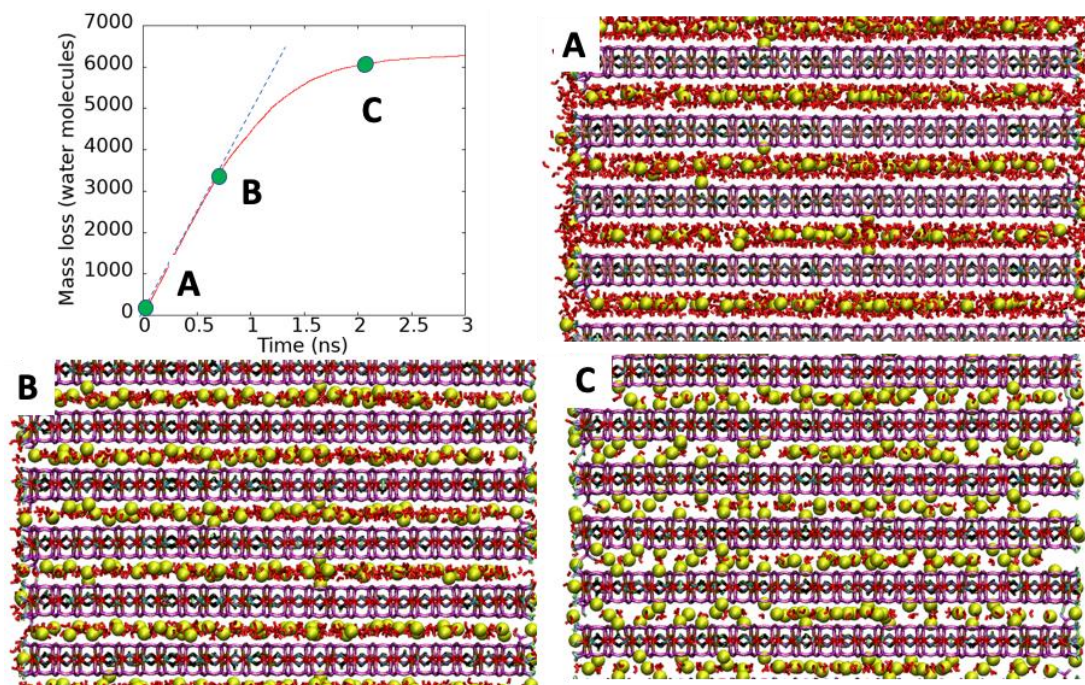


Figure 10. Mass loss (i.e., number of water molecules lost) as a function of simulation time (top left panel). Snapshots labeled A, B, and C are the configurations for the points A, B, and C marked in the top left panel, respectively. These snapshots represent the structural transformation of the Na-MMT particle during the dehydration process. The red line in the top left panel demonstrates the linear correlation between mass loss and time. The temperature is 30°C.

In Fig. 11 we report the simulation snapshots obtained from the dehydration simulations as a function of time to discuss the water transport pathway through the interlayer. At a specific time shown in Fig. 11, we report the side and top views of the interlayer. From the top view snapshots, we observed that  $\text{Na}^+$  ions (yellow spheres) tend to accumulate near the Mg atoms. Upon the dehydration, water (red) molecules that do not coordinate with  $\text{Na}^+$  ions evacuate first, resulting in vacuum sites inside the interlayer (see snapshots at 0.3 ns and beyond). In other words, the hydrophobic sites evacuate first, and the hydrophilic sites evacuate latter. The results in Fig. 11 also suggest that in the 1W hydration state (i.e., at 0.7 ns), water molecules distribution in the interlayer is not uniform (e.g., there are vacant and occupied sites). Therefore, the transition from 2W to 0W states does not necessarily go through the fully hydrated 1W hydration state (i.e., water molecules uniformly distributes in the interlayer). The water distribution in the interlayer (e.g., such as at 0.7 ns) will depend on surface charge and charge location. For high surface charge (i.e., high number of metal substitutions) and uniform charge distribution, water molecules might uniformly distribute in the interlayer. In our simulation the Mg:Al ratio of 0.75:3.25 leads to many vacant sites observed in the 1W hydration state at 0.7ns in Fig. 3.

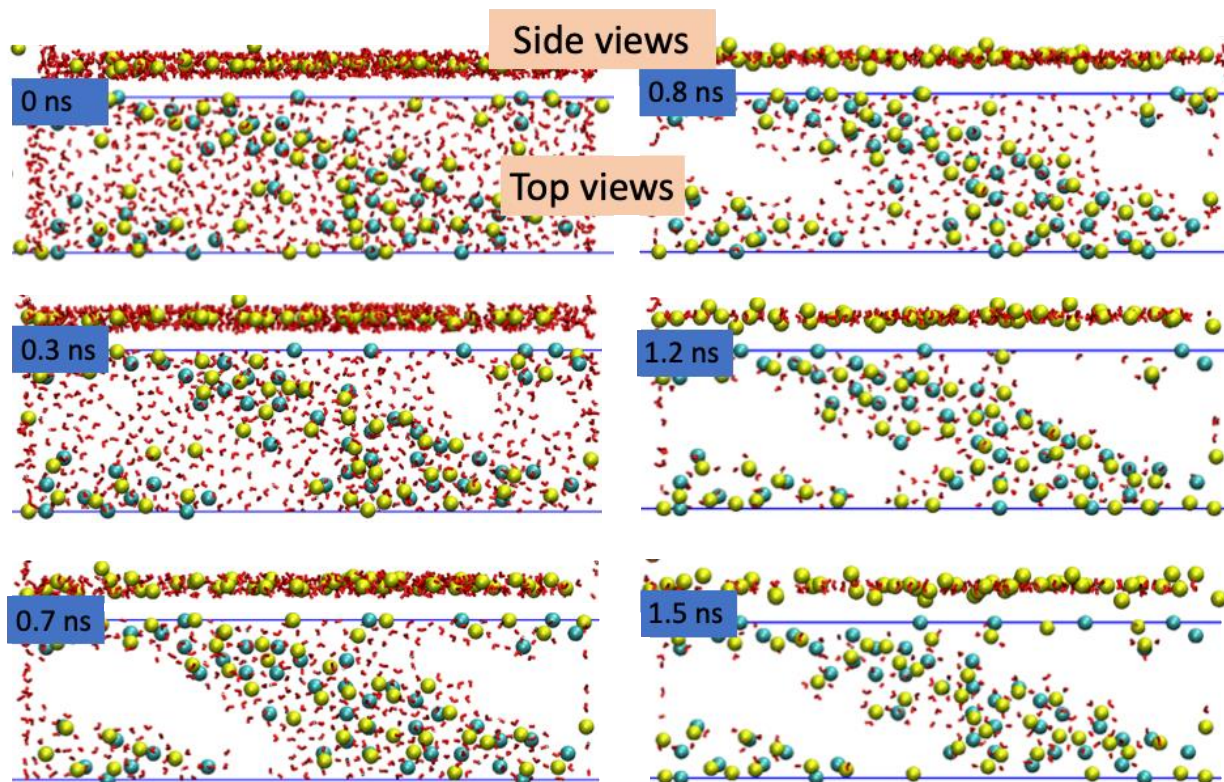


Figure 11. Simulation snapshots demonstrate water transport pathway through an MMT interlayer during the dehydration process. At a specific time, side and top views of the interlayer are reported. Cyan spheres are for Mg atoms of the MMT layer. See Fig. 1 for other color codes.

In Fig. 12A we report the d-spacing and water coordination number of  $\text{Na}^+$  ions as a function of the dehydration time (coordination number is the number of water molecules that are within  $3 \text{ \AA}$  from  $\text{Na}^+$  ions). The results indicate that at the beginning of the dehydration process the coordination number insignificantly decreases (green line, Fig. 12). This observation supports the result discussed in Fig. 11 that water molecules near the hydrophobic sites that do not coordinate with  $\text{Na}^+$  ions evacuate first. The subsequent steep decrease in the coordination number of  $\text{Na}^+$  atoms is an indication for the fast removal of water molecules belonging to the  $\text{Na}^+$  hydration shell. The steep decrease in the coordination number leads to a steep decrease in the d-spacing (red line). In other words, the collapse of the interlayer spacing from 2W to 1W (d-spacing  $\sim 12 \text{ \AA}$ ) structure associates with the fast water removal of about 3 to 4 water molecules from the  $\text{Na}^+$  hydration shell. Because of the steep decrease in coordination number, it is challenging to conclude if this short time period belongs to the first or second stage of the dehydration process. After this steep decrease, the coordination number and d-spacing slowly decrease as the dehydration process continues (Fig. 12B). This result indicates that the removal of the last 1-2 water molecules associated with the  $\text{Na}^+$  ion is very slow. The decrease of d-spacing from  $11.5 \text{ \AA}$  to that of 0W state is also very slow (Fig. 12B).

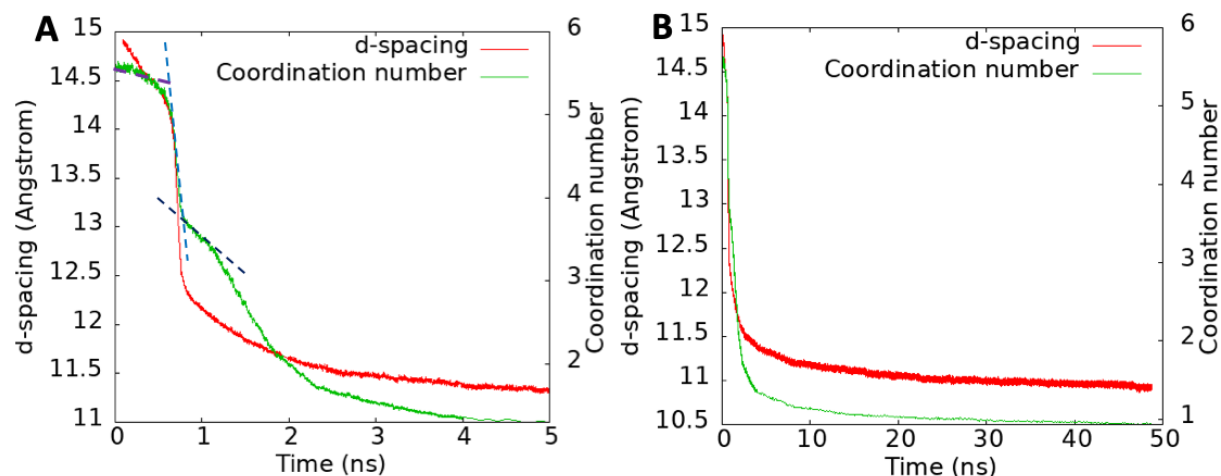


Figure 12. Coordination number of  $\text{Na}^+$  ions and d-spacing as a function of time for first 5 ns (A) and 50 ns (B) simulations. The dashed lines in panel A demonstrate the changes in the coordination number of  $\text{Na}^+$  ions during the dehydration process.

In Fig. 13 A, B, and C we report the mass loss, d-spacing, and water coordination number of  $\text{Na}^+$  ions during the dehydration process at  $30^\circ\text{C}$  and  $60^\circ\text{C}$  for 1W hydration state (see, snapshot in Fig. 13D). Note that water molecules uniformly distribute in the interlayer in Fig. 13D, unlike the water molecules distribution in 1W state shown Fig. 11 (both have the same d-spacing). We observe the same phenomenon described in Fig. 11 that the dehydration is a two-stage process (linear and non-linear mass loss. Because the number of water molecules available in the interlayer at 1W state is less than that in the 2W state the linear relation between mass loss and time (Fig. 13A) is observed for a very short time period (i.e., first 0.2 ns), and d-spacing and coordination number steeply decreases to around  $11.5 \text{ \AA}$  and 1.5, respectively. The removal of the last 1-2 water molecules from the  $\text{Na}^+$  ions is very slow. Similar to the dehydration process of 2W hydration state (Fig. 11), water molecules near hydrophobic sites evacuate first and leave hydrophobic sites unoccupied (e.g., snapshot at 0.5 ns in Fig. 13E). When the dehydration simulation is carried out at  $60^\circ\text{C}$ , we observe that the mass loss, coordination number, and d-spacing are the same with those at  $30^\circ\text{C}$  at the beginning of the dehydration process. The temperature seems to impact the diffusion stage, confirmed by the smaller d-spacing (Fig. 13B) and coordination number (Fig. 13C) at a later time in the dehydration process (e.g., at 2ns) for  $60^\circ\text{C}$ , compared to those at  $30^\circ\text{C}$ . The water diffusion and desorption are faster than those at  $30^\circ\text{C}$  leading to a higher mass loss in the late hydration process.

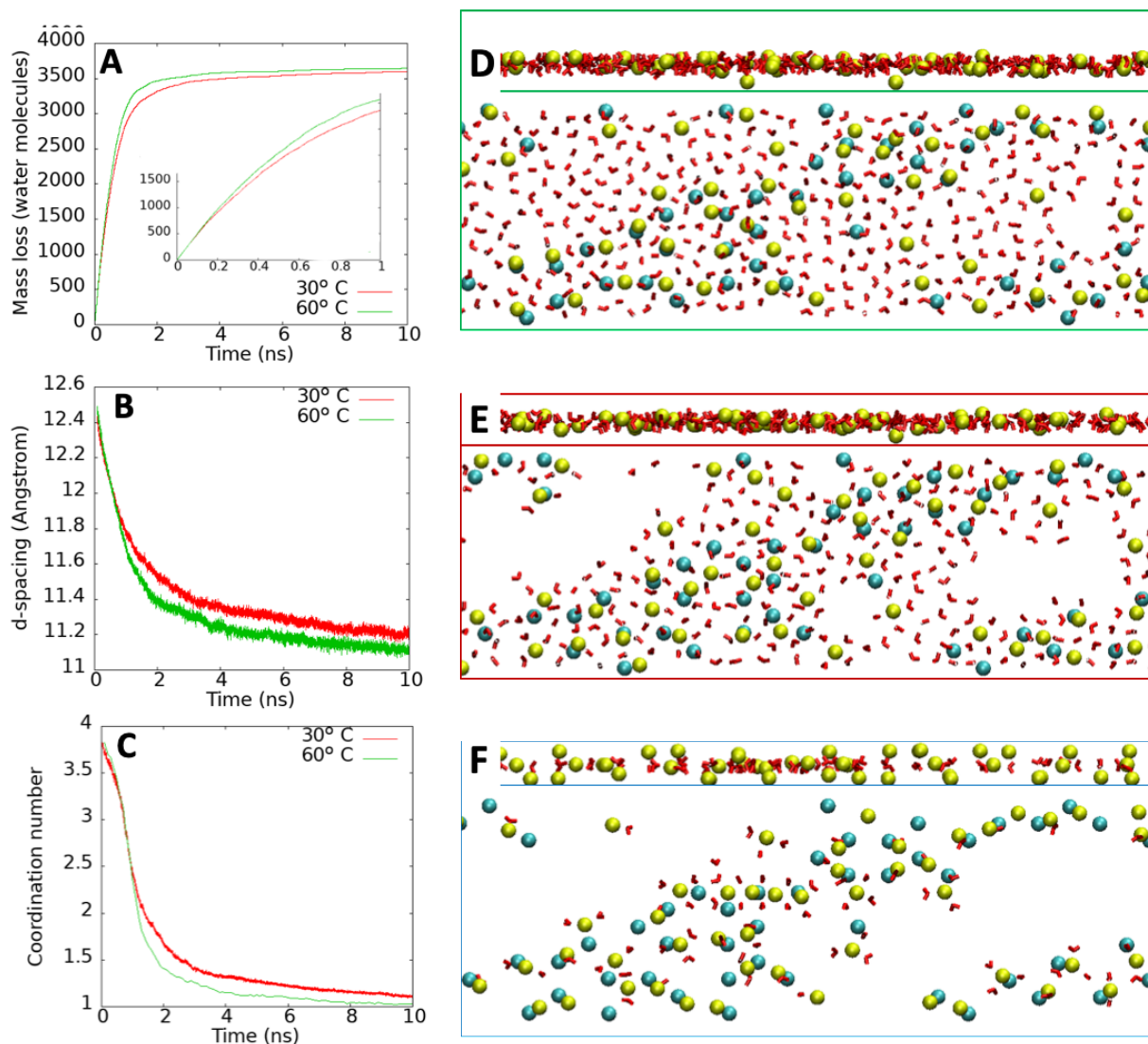


Figure 13. Mass loss (A), d-spacing (B), and water coordination number of  $\text{Na}^+$  ion (C) during the dehydration of 1W hydrated MMT at 30° and 60° C. Side and top views of the interlayers during the dehydration of 1W MMT at 0 (D), 0.5 (E), and 3 (F) ns at 30° C. See Figs. 9 and 10 for color codes

In Fig. 14 we present the experimental data for the heat flow, mass, and d-spacing as a function of dehydration time. Similar results obtained from thermogravimetric analysis were documented previously (Ho et al., 2020). At the beginning of the dehydration process there is 1 hydration layer (1W hydration state,  $\sim 12\text{-}12.5$  Å d-spacing as shown in Fig. 14A). On the time scale of Fig. 14A we observe that the d-spacing decreases quickly to  $\sim 11$  Å, and then more slowly after that. Even though there are huge differences between temporal and spatial scales in MD with those in experiment, the behavior of the d-spacing is consistent with two-stage process observed in the MD simulation (see Fig. 13B). The sample mass decreases relatively rapidly at the beginning and more slowly afterward (Fig. 14B), which is also supported by our simulation result (Fig. 13A). There is a large endothermic peak in the DSC about 1.5h into dehydration (accompanied by an increasing rate of mass loss in the TGA), that is associated with the steep decrease in the coordination number of the interlayer ions (or fast desorption of water from the  $\text{Na}^+$  ion hydration shell), which is also supported by our MD result observed in Fig. 13C.

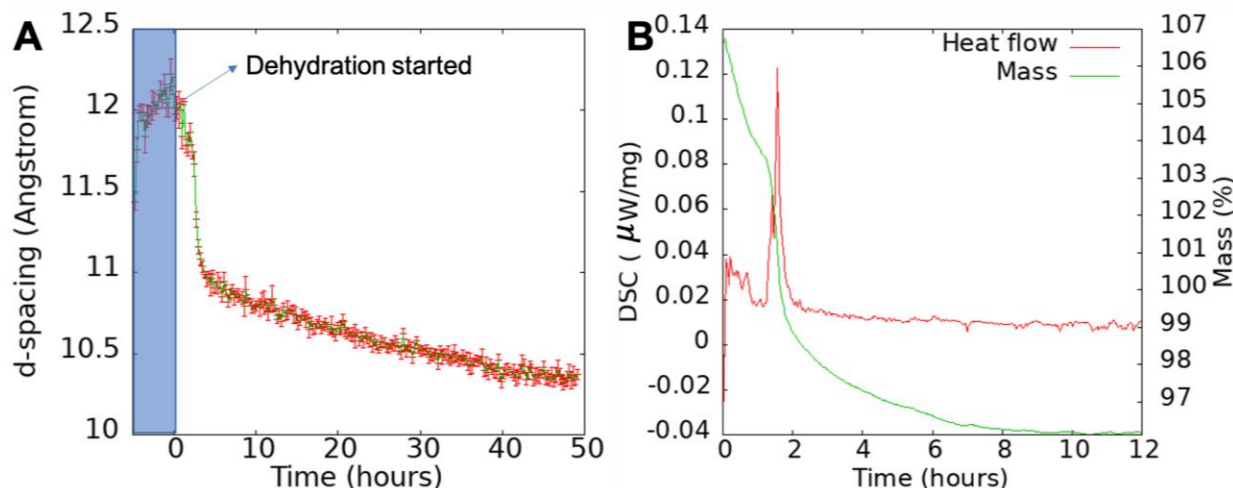


Figure 14. d-spacing (A) and heat flow and mass (B) as a function of time at 60 °C. The sample was hydrated at 50% RH (60 °C) for several hours. At the beginning of the dehydration process the RH was reduced to 0%. More details can be found in the method and our previous report (Ho et al., 2020).

## Conclusions from the MD Study

Using molecular dynamics simulations, we demonstrate that clay dehydration is a two-stage process. In the first stage, water transport exhibits an advection mechanism as mass loss is linear with time. The first stage is associated with the evacuation of water molecules from the hydrophobic sites and also with the fast removal of the first few water molecules from the  $\text{Na}^+$  ion hydration shell. The second stage represents the slow desorption of the last 1-2 water molecules from the  $\text{Na}^+$  ions. Movement of water molecules through the interlayer in the second stage follows a diffusion mechanism. These conclusions are supported by our results obtained from TGA/DSC calorimetry, and in-situ XRD experiments.

## V. 1D Reactive-Transport Modeling of Sedimentary Rock Leaching Experiments

### Introduction

Matteo et al. (2019) described 1D PFLOTRAN reactive-transport simulations for the idealized case of cement-clay interactions with emphasis on the clay rock / cement interface. The role of barrier interfaces in seal performance and interactions with other barrier materials is crucial to the barrier isolation function in deep geological nuclear waste repositories (Berner et al., 2013; Gaboreau et al., 2012; Kosakowski and Berner, 2013; Soler, 2012; Soler and Mader, 2010). The effects of porosity enhancement and reduction (i.e., clogging) due to mineral dissolution/precipitation have been the focus in various reactive-transport modeling efforts including benchmark test cases for computer code inter-comparisons efforts (Marty et al., 2015; Xie et al., 2015). The main purpose behind these computational reactive-transport modeling efforts lies in the complex coupling of geochemical interactions (kinetic vs. transport controlled) for the most part involving reactive diffusion phenomena in porous media (Marty et al., 2015). The extent to which these models capture relevant physico-chemical processes with enough realism and adequacy still needs to be examined and reconciled with the limited amount of available field and experimental laboratory data.

Leaching behavior of barrier materials whether engineered or natural provides key chemical and structural characterization data of (geo)chemical interactions at interfaces. Such data is useful in the evaluation and testing of reactive-transport models such as described in Matteo et al. (2019) for cement-clayrock interactions and those described for DECOVALEX19 Task C on the GREET experiment (Jové Colón et al. 2020) where kinetic rate (e.g., solid dissolution), transport length scale, and diffusion parameters can have an effect on representing the temporal change in measured solute concentrations. In this work, a 1D PFLOTTRAN reactive-transport simulation will be conducted to simulate leaching of a marl rock from the carbonate Ghareb and Nezer Formations in the northern Negev, Israel (Klein-BenDavid et al., 2019). The controlled leaching experiment of a carbonate-rich sedimentary rock with minor clay offers the opportunity of using leaching data to test this type of simulation in the presence of complex carbonate equilibria. When combined with cement at an interface, marl interactions can play a key role on cement carbonation under alkaline conditions.

### Marl Rock Properties

The marl samples were obtained from the Yamin Plateau, northern Negev desert, in Israel specifically from the carbonate-rich Mount Scopus Group. This formation group are of Upper Cretaceous to early Paleocene age. The bulk mineralogy of the marl samples have been estimated by X-Ray diffraction (XRD) – see Table 1. The volume fractions were determined from mineral densities and the porosity of the marl sample (32%).

Table 1. Mineral volume fractions based on XRD data.

Mineral	Volume Fraction	Fraction (XRD)
Calcite	0.643	0.95
Quartz(alpha)	7.004E-03	0.01
Kaolinite	0.0212	0.03
Halite	7.537E-04	<0.01*
Sylvite	2.70E-05	<0.01*
Total	0.672	1

\* Estimated, not measured by XRD. Halite and sylvite volume fractions were determined from fitting solute concentrations vs. time profiles from the PFLOTTRAN 1D reactive-transport simulation. These estimates were used as a source of Na and K in the marl pore solution to account for small amounts of salt in the pores.

### Monolith leaching test (EPA Method 1315)

Matteo et al. (2020) describes the EPA method 1315 used in the rock monolith leaching test. The description will be duplicated here for completeness. The EPA Method 1315 is a mass transfer rate, tank leaching test (U.S. EPA, 2017). The test consists of continuous leaching of



water-saturated monolithic material with periodic renewal of the eluent at predetermined intervals. The concentration of constituent in each interval eluate is used to calculate the interval mass flux across the exposed surface area ( $\text{mg m}^{-2} \text{sec}^{-1}$ ) and the cumulative mass release ( $\text{mg m}^{-2}$ ) to the eluate. The marl leaching tests were conducted at Vanderbilt University. After each eluant exchange, the eluate is analyzed for pH, conductivity, Eh, elemental analysis by ICP-MS (EPA Method 6020B) and inductively coupled plasma optical emission spectroscopy (ICP-OES; EPA Method 6010D), dissolved organic carbon (DOC), and other parameters of interest. DOC was analyzed using Shimadzu TOC-V CPH/CPN (Shimadzu Scientific Instruments, Inc., Columbia, MD) by catalytic oxidation/non-dispersive infrared detection (NDIR) following EPA Method 9060A.

Test samples for Method 1315 were prepared by cutting approximately 2.5-cm cubes from the larger rock specimens utilizing a rock saw with a diamond blade. The 2.5-cm cubes were then cast in epoxy utilizing 5-cm by 10-cm tubes for molds and epoxy resin and hardener (Fig. 15). After the samples were set, they were demolded and polished. Samples were polished using 140 grit paper for coarse polishing to expose the surface of the sample and 240 grit paper for finer polishing. Samples were then exposed under 100% relative humidity at 30°C in an environmental chamber for approximately three weeks to achieve water saturation through capillary condensation of water vapor. Samples were weighed approximately every 48 hours until constant weight indicated that saturation was achieved (approximately 2 weeks). Fig. 15a show the hand rock specimens and the epoxy mounted samples along with the experimental leaching tank apparatus.

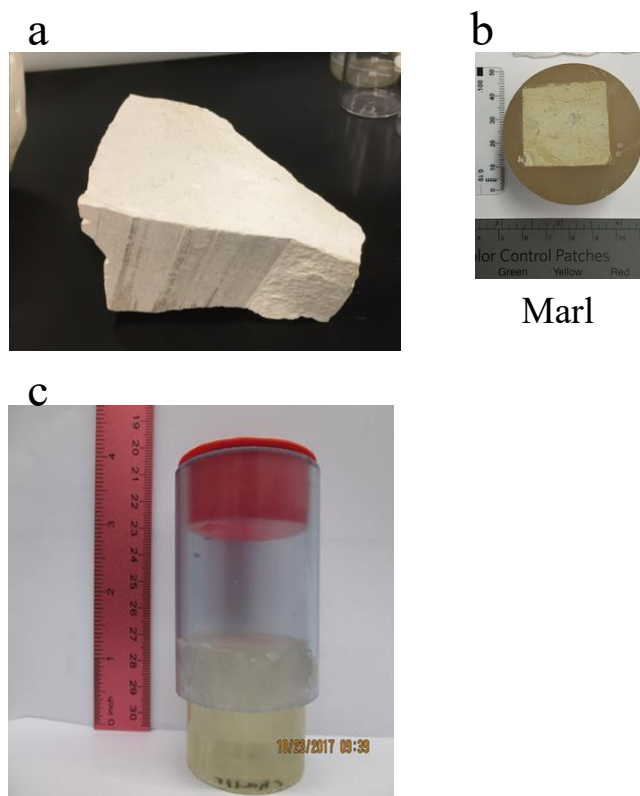


Figure 15. (a) Bulk rock sample; (b) epoxy-mounted sample used for 1315, and (c) experimental set up for the 1315 test.

## 1D PFLOTRAN Reactive Transport Simulations

The PFLOTRAN simulator (<https://www.pflotran.org>) is an open source, state-of-the-art massively parallel computer code to perform calculations for subsurface single- and multi-phase flow and reactive transport under (non)isothermal conditions. The code is designed for use on massively parallel or high performance computing (HPC) platforms where efficient scalability becomes important for large coupled process problems. Lichtner et al. (2013) provides details on PFLOTRAN simulation capabilities, reactive-transport formulations, and geochemical treatment of mineral-fluid interactions. The THERMOTDEM thermodynamic database (Blanc et al., 2012; Blanc et al., 2006) was used in the simulations.

The structured mesh discretization is defined by a rectangular geometry with dimensions consistent with those of the marl sample in the leaching experiments (Fig. 16). The solid monolith meshed domain is composed of 43 cells (bottom) and a single cell (top) for the leaching bath solution. The surrounding epoxy mount is considered to be inert and thus is not part of the meshed domain. No flow boundary conditions are imposed on the faces of the rectangular domain. Small pressure perturbations in the leaching solution upper “box” are allowed for some “mixing”.

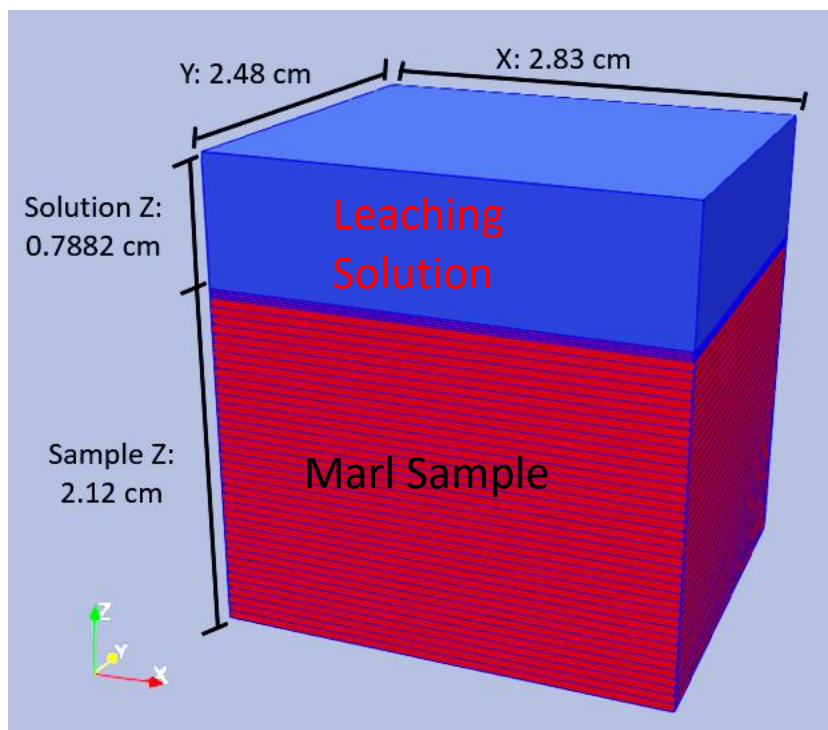


Figure 16. Mesh discretization of the solid (lower) and leaching solution (upper) domains along with dimensions of the rectangular domain. The marl sample meshed domain is composed of 43 cells and a single cell for the leaching solution.

As mentioned earlier, the porosity of the marl is 32%, with a permeability of  $1 \times 10^{-16} \text{ m}^2$ , and unit tortuosity (Table 2). The 1D diffusion problem is isothermal at  $25^\circ\text{C}$  with a diffusion coefficient of  $2.5\text{E-}10 \text{ m}^2/\text{s}$ . The diffusion coefficient was adjusted to fit the Na and K solute

concentration vs. time profiles. Updates to permeability and porosity at each time step as a result of chemical interactions were considered in the simulations.

Table 2. Marl monolith properties

Parameter	Value
Porosity	0.32
Tortuosity	1
Rock Density	1947 kg/m <sup>3</sup> *
Permeability (Isotropic)	1.0E-16 m <sup>2</sup>

\* Derived from sample mass and dimensions.

The mineral reactive surface areas (RSAs) were set to unity except for calcite and sylvite. The former has a value of 1000 m<sup>2</sup>/m<sup>3</sup> rock whereas the latter has a value of 0.1 m<sup>2</sup>/m<sup>3</sup> rock. The reason for the large RSA value for calcite is to scale up its dissolution as an attempt to evaluate peak Ca concentrations early in the experiments. A transition state theory (TST) rate law implemented in PFLOTTRAN was adopted for calcite dissolution using a rate constant value of 1.778E-05 mol/m<sup>2</sup> s. The TST model is with Ca<sup>++</sup> as the prefactor species and whose activity term in the equation has unity exponent. The TST model was also used for kaolinite with a far from equilibrium dissolution rate constant of 1.12E-14 mol/m<sup>2</sup> s where H<sup>+</sup> is the prefactor species and the activity term has an exponent of 0.1. Far from equilibrium dissolution rate constants for quartz (alpha), halite, and sylvite are constrained to 5.0E-14 mol/m<sup>2</sup> s, 2.5E-03 mol/m<sup>2</sup> s, and 2.5E-02 mol/m<sup>2</sup> s, respectively.

The initial marl pore solution chemistry is taken as very dilute in all its components where the Ca<sup>++</sup> concentration is 3.2E-05 M, constrained to match initial concentrations in the leachate solution. HCO<sub>3</sub><sup>-</sup> concentration is constrained by charge balancing with initial pH 7. The dilute pore solution reacts rapidly in the initial steps of the simulation. The leaching solution or eluent chemistries at each renewal interval were obtained from Drs. Chen Gruber and David Kosson at Vanderbilt University. Blank solutions for these experiments (solutions reacting with epoxy mount without monolith sample) show excess silica that originated from the sealant use to hold the mold cast. As described previously, these eluent solutions are periodically renewed in the experiment. This excess silica concentration was corrected in the input leaching solutions. The chemistry of leaching solutions for each replenishments in the tank bath cell at the corresponding times are specified in the PFLOTTRAN input deck.

### Preliminary Results and Discussion

Fig. 17 shows the change in pH and Ca<sup>++</sup> concentration with time for the 1315 leaching experiment and the PFFLOTTRAN 1D reactive-transport simulation. The overall pH trend is represented by the model except for deviations in the initial and final stages of the experiment. The initial drop in pH illustrated by the experimental data cannot be represented by the model. Similarly, the rapid initial increase and peak Ca<sup>++</sup> concentration from the experiment is not described by the simulation. However, there is good agreement in predicted pH at later times (from ~950 to ~2700 hours). In an analogous manner, the predicted Ca<sup>++</sup> concentrations are

good agreement with the experimental data. The overall discrepancies in the pH and  $\text{Ca}^{++}$  concentration trends at these later times are considered reasonable given the nature of the experiment where multiple leachate solution batches (from periodic eluent renewals) are sampled at various times.

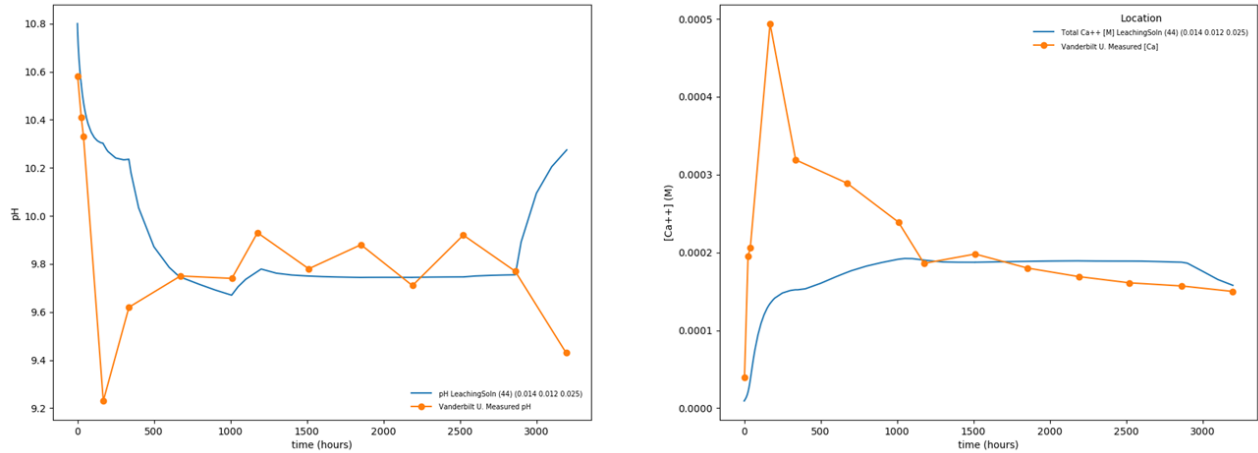


Figure 17. Temporal change of pH (left panel) and total  $\text{Ca}^{++}$  concentration (right panel) in leachate solutions for the 1315 leaching experiment. The light blue solid line stands for the 1D PFLOTTRAN simulation and the connected filled orange circles represents the experimental results.

Fig. 18 shows the change in total dissolved Si concentration with time depicting an overall trend in good agreement with the experimental data. It should be noted that dissolved Si concentration in the leaching solution needed to be corrected because of contamination with sealant. Similar to pH and  $\text{Ca}^{++}$  concentration trends, the initial rapid increase and peak Si concentrations are not predicted by the model. Still, there is good agreement in the overall trend and the experimental data at later times.

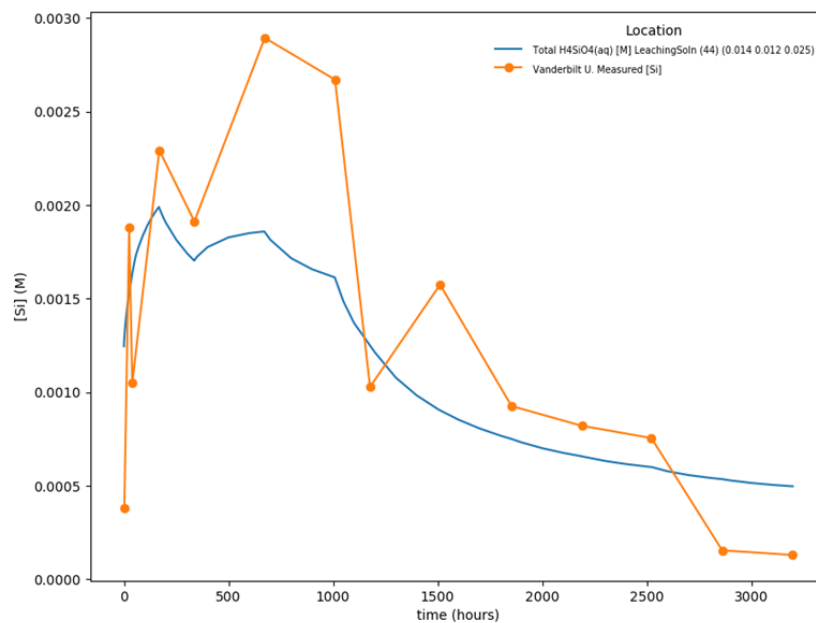


Figure 18. Temporal change of total dissolved Si concentration. The initial Si concentration in the input leaching solutions needed to be corrected due to contamination from the experimental setup.

Fig.18 shows the change in total dissolved Na and K concentrations with time where simulation results are in excellent agreement with the experimental data. These Na and K concentration vs. time profiles were used to constrain the diffusion constant adopted in the model. The origin of Na and K in the marl is attributed to minor amounts of salt represented in the model by halite (NaCl) and sylvite (KCl). It is inferred that evaporative conditions in the formation of the marl rock could cause salt precipitation in the pores. Given the similarity in the overall trends of these two curves to that of the  $\text{Ca}^{++}$  concentration profile at initial times may suggest the rapid dissolution of potential Ca-bearing salt. However, no Ca-bearing salt was identified in the XRD analysis or in the marl rock mineralogy. Another potential reason for having rapid initial increases and peak solute concentrations is the fast dissolution of fine material on the surface as a result of polishing.

This study is still work in progress where more parameter sensitivities need to be evaluated. The current results show that the PFLOTRAN 1D reactive-transport model implementation of the EPA 1315 monolith leaching test can represent the overall trends of temporal changes of solute concentration profiles based on the major rock constituents. In addition to the evaluation of parameter sensitivities, other work includes effects of meshing discretization and evaluation of  $\text{pCO}_2(\text{g})$  on carbonate interactions. Testing the implementation of this 1D reactive-transport simulation approach is planned for cement-rock leaching scenarios.

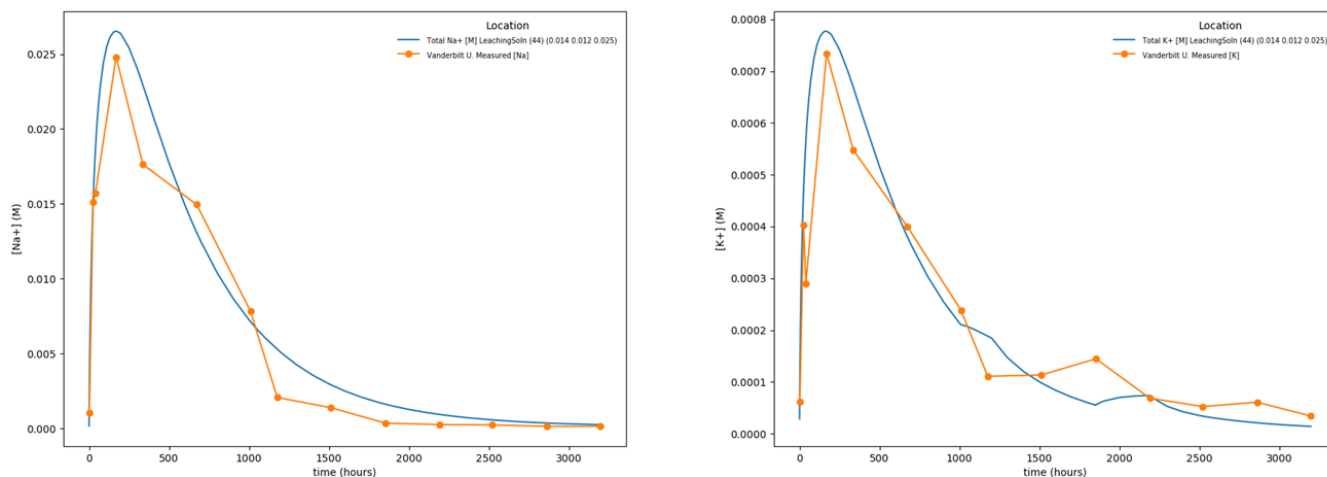


Figure 18. Temporal change of Na (left panel) and K concentration (right panel). Notice the very good agreement between model prediction and experimental data.

## VI. HotBENT Heated Column Experiment: Preliminary XRD Analysis of Post-Experiment Bentonite Samples

The HotBENT heated/unheated tests on packed on MX-80 bentonite columns is a laboratory-scale experiment conducted at LBNL in support of the HotBENT field-scale heater test at the Grimsel Test Site (GTS), Switzerland. The objectives of the HotBENT heater test are to study long-term THMC behavior of bentonite backfill behavior at elevated temperatures of 200°C. The laboratory-scale experiment permits the use of monitoring and characterization methods that would otherwise be either difficult to deploy, implement, or operate at the field scale. The main goals of this laboratory-scale heater column experiments are to improve our knowledge of bentonite THMC behavior at elevated temperatures under controlled hydration conditions,

perform comparisons between laboratory- and field-scale experimental heater test results, and develop an experimentation platform to conduct bentonite barrier studies at high temperatures (Zheng et al., 2020). Details of the experimental setup and operations for both heated and unheated columns are given by Zheng et al. (2020).

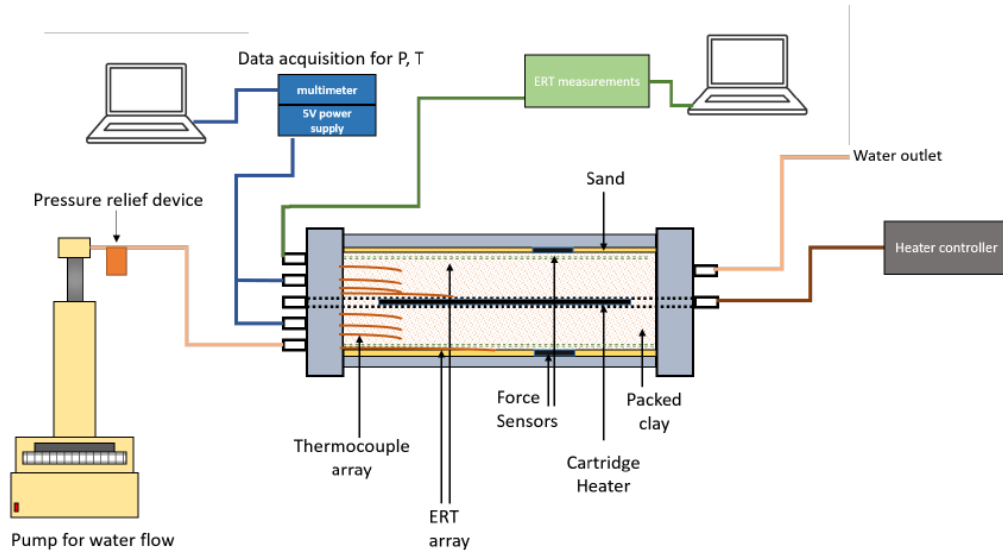


Figure 19. Schematic diagram of the entire experimental column setup including flow control, sensors, and cartridge heater at the column center axis. The sand layer between the clay and vessel wall is used to hydrate the bentonite by continuous brine flow. The inner diameter (ID) of the column is 6.5 inches, outer diameter (OD) is 7.5 inches, and the height is 18 inches (Zheng et al., 2020).

The columns experiments (Fig. 19) were conducted at a temperature of 200°C with continuous sensor monitoring for 255 days. After the experiment shutdown, samples were collected from different radial regions of the column for subsequent chemical analysis and moisture content (Fig. 20). The next section will provide preliminary XRD data of post-experiment bentonite samples.

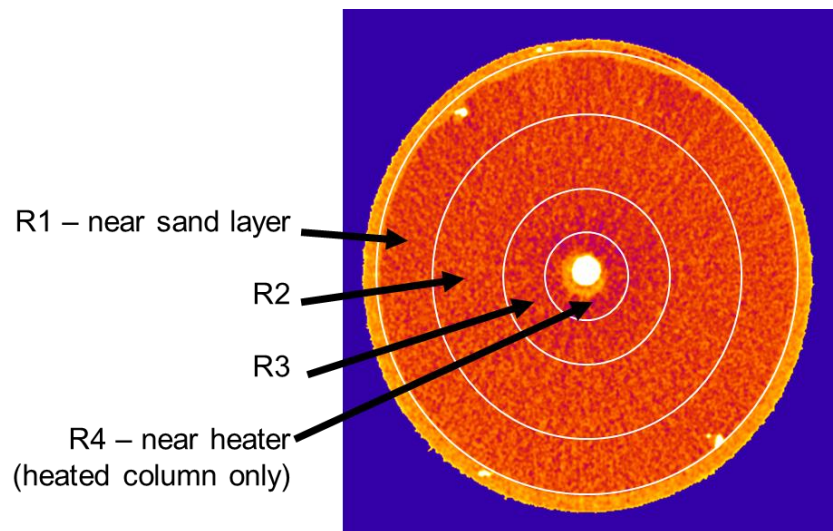


Figure 20. CT scan image showing the column cross section delineating the sampling radial zones. The outer orange color rim is the sand layer (Figure courtesy of Liange Zheng and Sharon Borglin – LBNL).

## Preliminary XRD Analyses of Post-Experiment Bentonite Samples

SNL obtained samples for regions R1, R2, and R3 (Fig. 20) for both heated and unheated columns from sieved size fractions of <38 microns. These samples were prepared for oriented air-dried (AD) and ethylene glycol (EG) saturated samples. Sample preparation consisted first of crushing the clay using a mortar and pestle into small particle sizes to achieve a “powder like” consistency. The samples were subsequently sieved to < 75  $\mu\text{m}$  and < 38  $\mu\text{m}$  particle size. The < 38  $\mu\text{m}$  particles were used to make XRD mounts. XRD analysis of air-dried clay sample consisted of adding ~0.1 g of clay to a 5 mL scintillation vial. 2 mL of a 70-30% water-ethanol mixture was added to the scintillation vial to have a mass/liquid ratio of 0.05. The ethanol was added to the samples to decrease the cracking behavior of the oriented clay samples upon drying. The suspended clay was hand shaken vigorously until clay was sufficiently suspended and sonicated with a benchtop microtip sonicator for approximately 1 minute. Then using a 1000  $\mu\text{L}$  micropipette the slurry was pipetted in a circular motion onto the zero-background silicon wafer. The oriented mount was placed on the countertop at ambient conditions, parafilm and allowed to air-dry completely (overnight). After the sample had completely dried, the wafer was placed in the Bruker D2-Phaser sample holder to perform the XRD analysis. After completion of XRD analysis of the dried samples, this bentonite material was then placed into a desiccator over a pool of ethylene glycol. The desiccator was then placed in the oven heated at 60°C overnight to ensure glycol saturation of the bentonite samples. The following day the sample was removed from the desiccator and the XRD analysis was conducted immediately to ensure the bentonite remained glycol saturated. The powder diffraction data was collected using a Bruker D2 Phaser benchtop diffractometer with a  $\text{CuK}\alpha$  (1.54 Å) X-ray wavelength. The analysis was conducted in a 2-theta range of 3 -70° with 0.5 s time per step. This resulted in XRD runs that were ~23.5 minutes in duration. Silicon wafers were chosen as the sample holders for the oriented clay mounts as it provides very low background interference and were optimal for making oriented clay slurry mounts. A desiccator was adapted into a glycolation chamber for the purposes of the project by filling the desiccator with ethylene glycol, then heating the entire desiccator at 60°C - the sample was placed on a petri dish above the layer of ethylene glycol at the bottom of the desiccator. The heat caused the ethylene glycol to vaporize and create a glycol vapor saturated environment within the desiccator.

These XRD analyses were conducted very recently and any evaluation of the data is very preliminary. Fig. 21 shows stacked XRD spectra of bentonite sampled in region R3 (closer to the heater) for both heated (V1) and unheated (V2) column experiments. As expected, there is a close correspondence of montmorillonite peaks with PDF cards for the EG samples. Other strong peaks such as those for quartz are also identified. The appearance of a 10 Angstrom peak at 2-theta of ~9 degrees in both heated/unheated EG samples may be indicative of potential interstratified illite in the clay but this needs much further evaluation of the XRD spectra. The study of Gomez-Espina and Villar (2016) suggested the presence of interstratified illite in heated column experiments using MX-80 bentonite. Other features in the XRD spectra are peak broadening at 2-theta 6-9-10 degrees in the AD samples with increasing distance from the column center axis (regions R1 and R2) as observed in Figs. 22 and 23. The regions R1 and R2 are closer to the sand layer which are expected to be more hydrated in the heated (V1) column. Such peak broadening of the 2-theta range of 6-9-10 degrees has been observed from *in situ* XRD measurements under controlled temperature and moisture conditions. Again, more work is needed to evaluate the structural data to assess the changes in bentonite hydration/dehydration under variable temperature and moisture conditions.

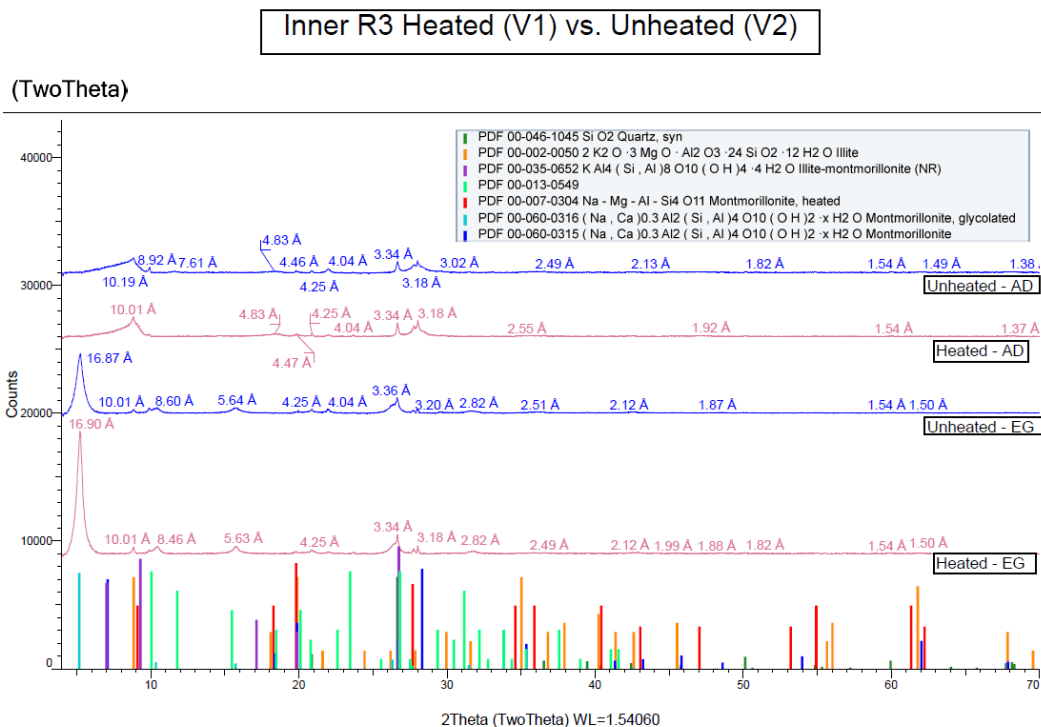


Figure 21. XRD stacked spectra of bentonite sampled in region R3 (closer to the heater) for both heated (V1) and unheated (V2) column experiments. AD stands for air-dried and EG denotes ethylene glycol saturated samples. Vertical axis scale are arbitrary counts.

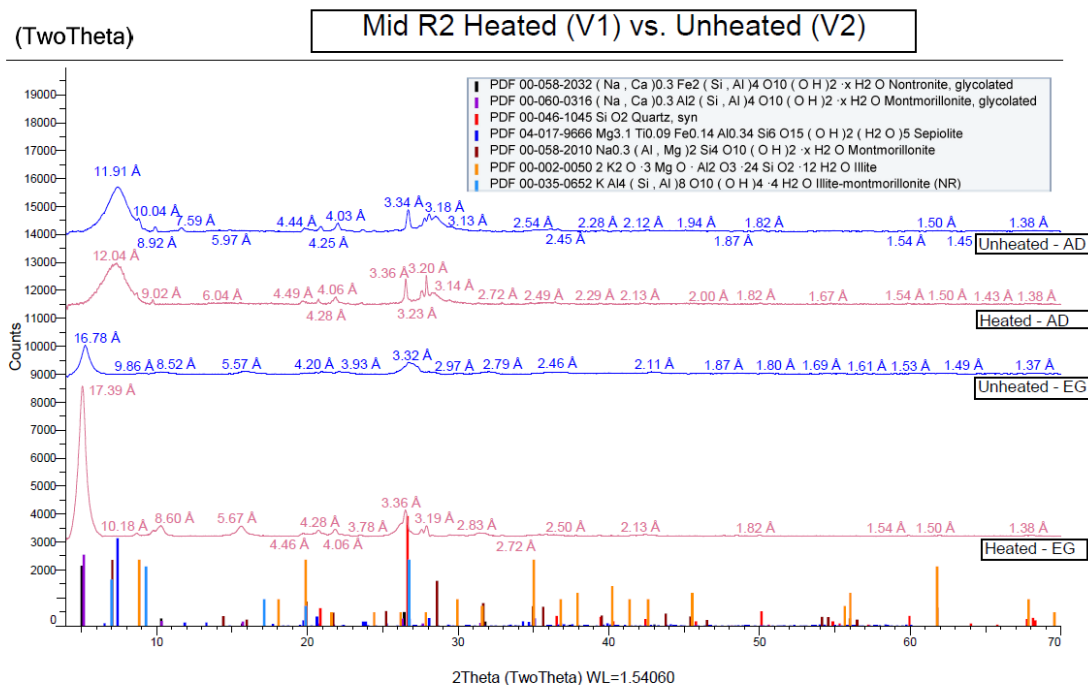


Figure 22. XRD stacked spectra of bentonite sampled in region R2 (midpoint) for both heated (V1) and unheated (V2) column experiments. AD stands for air-dried and EG denotes ethylene glycol saturated samples. Vertical axis scale are arbitrary counts.



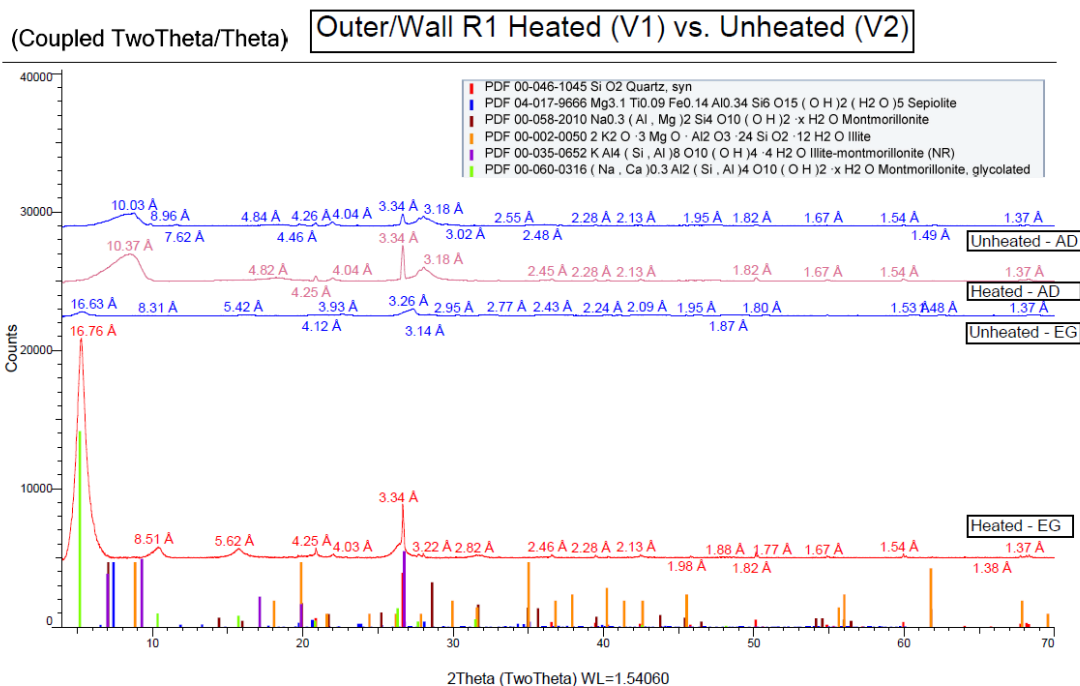


Figure 23. XRD stacked spectra of bentonite sampled in region R1 (outer) for both heated (V1) and unheated (V2) column experiments. AD stands for air-dried and EG denotes ethylene glycol saturated samples. Vertical axis scale are arbitrary counts.

## VII. Conclusions

### • FEBEX-DP:

- Results from continuing cyclical TGA/DSC thermal analyses under controlled RH (hydration/dehydration) at elevated temperatures (85°C and 150°C) for FEBEX-DP Section 49 samples have been obtained.
- The overall thermal behavior is similar to some extent for previous experiments at 60°C. However, trends for extended hydration periods (>120 minutes) at high temperatures no longer follow the trend of lower hydration periods and need to be investigated further. Still, the cyclical thermal analysis indicates that the dehydration behavior is a function of the duration of hydration that precedes it.
- Molecular dynamics (MD) simulations demonstrate that clay dehydration is a two-stage process. The first stage of water transport exhibits an advection mechanism as mass loss is linear with time. The first stage is associated with the evacuation of water molecules from the hydrophobic sites. The second stage represents slow desorption of the last 1-2 water molecules from the Na<sup>+</sup> ions leading to a diffusion mechanism. These conclusions are supported by our results obtained from TGA/DSC calorimetry, and in-situ XRD experiments on FEBEX-DP bentonite samples.

### • Reactive-Transport Modeling of Barrier Material Leaching

- The PFLOTTRAN 1D reactive-transport model implementation of the EPA 1315 monolith leaching test or marl rock generated encouraging results representing

the overall trends of temporal changes in solute concentration profiles based on the major rock mineral components.

- In addition to the evaluation of parameter sensitivities, future work include will include the effects of meshing discretization at the interface, evaluation of  $p\text{CO}_2(\text{g})$  on carbonate interactions, and further testing of the 1D simulation approach rock-cement leaching.
- **LBNL HotBENT Heated/Unheated Column Test: Preliminary XRD analyses of post-experiment Samples**
  - Preliminary XRD analyses (AD and EG) were conducted on post-experiments samples collected at various radial distances from the central heating element. This analyses include samples from heated and unheated columns. Work is planned for additional XRD analyses and evaluation of the data.
  - The XRD spectra shows close correspondence to the montmorillonite peaks, as expected, for AD and EG samples. Although there are some commonalities in the XRD spectra for samples from both heated and unheated columns, there are also some differences such as peak broadening in samples radially farther from the column central axis.

## VIII. FY22 Work

Planned work on **FEDEX-DP** samples for FY22 (and the remainder of FY21):

- The focus for the remainder of FY21 is to evaluate the collected data at high temperatures (85°C and 150°C), focusing on the trend loss in the temporal DSC data with increasing clay hydration periods.
- Continue cyclical thermal analyses conducted at higher temperatures and controlled moisture conditions to evaluate the effect on hydration/dehydration profiles. There are also plans to continue the *in situ* XRD analyses under controlled moisture and temperature conditions as soon as the equipment setup becomes available. There are also plan into extending thermal analyses into other types of bentonite clay material.
- Expand MD simulations on dehydration phenomena at the clay interlayer.
  - Expand the work on montmorillonite dehydration in the presence of  $\text{K}^+$  and  $\text{Ca}^{++}$
  - Evaluate the effects of surface charge density on montmorillonite dehydration and water transport
  - Exploratory studies of  $\text{H}_2(\text{gas})$  adsorption and transport/mobility in the interlayer of clay (wet, or dry) through MD simulations
  - Thermodynamic analysis of clay hydration and dehydration from MD simulations

Planned work on international collaborations work for FY22 (and the remainder of FY21):

- Continue (1D) PFLOTTRAN reactive-transport modeling of leaching of rock (monolith) and cement experiments. This activity is done in concert with the EBS work package. This offers an unique opportunity of exploiting existing leaching data on barrier phases to test existing simulation approaches for hydro-chemical (HC) couplings.
- LBNL HotBENT Heated/Unheated Column Experiments

- Continue XRD analyses of both column experiments and evaluation of collected data
- Plans to conduct X-ray fluorescence (XRF) compositional analysis of collected samples.
- Explore the possibility of conducting TH and THC PFLOTTRAN simulations of the LBNL column experiment as part of the SKB TF. The limitation of the PFLOTTRAN simulator is the lack of mechanical modeling capability.
- Explore the application of PFLOTTRAN to DECOVALEX2023 Task D (Honorobe URL) for the S1-3 bentonite infiltration and maybe the S1-1 bentonite swelling pressure test. The latter will be assessed from clay hydration properties but these are not considered by the Task D teams.

## IX. References

Amato, I. (2013) Green cement: concrete solutions. *Nature news* 494, 300.

Arthur, M.A. and Cole, D.R. (2014) Unconventional hydrocarbon resources: prospects and problems. *Elements* 10, 257-264.

Babu, J.S. and Sathian, S.P. (2011) The role of activation energy and reduced viscosity on the enhancement of water flow through carbon nanotubes. *The Journal of chemical physics* 134, 194509.

Berner, U., Kulik, D.A. and Kosakowski, G. (2013) Geochemical impact of a low-pH cement liner on the near field of a repository for spent fuel and high-level radioactive waste. *Physics and Chemistry of the Earth, Parts A/B/C* 64, 46-56.

Birkholzer, J., Faybishenko, B., Ajo-Franklin, J., Borglin, S., Dobson, P., Gilbert, B., Guglielmi, Y., Fox, P.M., Kim, K., Nico, P., Rutqvist, J., Sonnenthal, E., Xu, H., Wu, Y., Zheng, L., Caporuscio, F.A., Reimus, P., Viswanathan, H., Jove-Colon, C.F., Wang, Y., Kuhlman, K., Matteo, E., McMahon, K. and Zavarin, M. (2019) International Collaboration Activities in Different Geologic Environments, Spent Fuel Waste Science and Technology (SFWST) Deliverable M2SF-19LB010307012 (LBNL-2001239). Lawrence Berkeley National Laboratories (LBNL), Berkeley, CA USA, 356 pp..

Blanc, P., Lassin, A., Piantone, P., Azaroual, M., Jacquemet, N., Fabbri, A. and Gaucher, A., (2012) Thermoddem: A geochemical database focused on low temperature water/rock interactions and waste materials. *Applied Geochemistry*, 27: 2107-2116.

Blanc, P., Piantone, P., Lassin, A. and Burnol, A., (2006) Thermochimie: Sélection de constantes thermodynamiques pour les éléments majeurs, le plomb et le cadmium, Rapport final BRGM/RP-54902-FR BRGM, France, pp. 1-157.

Busch, A., Alles, S., Gensterblum, Y., Prinz, D., Dewhurst, D.N., Raven, M.D., Stanjek, H. and Krooss, B.M. (2008) Carbon dioxide storage potential of shales. *Int J Greenh Gas Con* 2, 297-308.

Chang, F.-R.C., Skipper, N. and Sposito, G. (1995) Computer simulation of interlayer molecular structure in sodium montmorillonite hydrates. *Langmuir* 11, 2734-2741.

Chen, X., Cao, G., Han, A., Punyamurtula, V.K., Liu, L., Culligan, P.J., Kim, T. and Qiao, Y. (2008) Nanoscale fluid transport: size and rate effects. *Nano letters* 8, 2988-2992.

Cheshire, M.C., Caporuscio, F.A., Jové Colón, C.F., and Norskog, K.E. (2018). "Fe-saponite growth on low-carbon and stainless steel in hydrothermal-bentonite experiments." *Journal of Nuclear Materials* 511: 353-366.

Clark, G., Grim, R. and Bradley, W. (1937) A study of the behavior of montmorillonite upon wetting. *Zeitschrift für Kristallographie-Crystalline Materials* 97, 216-222.

Cygan, R.T., Liang, J.-J. and Kalinichev, A.G. (2004) Molecular models of hydroxide, oxyhydroxide, and clay phases and the development of a general force field. *The Journal of Physical Chemistry B* 108, 1255-1266.

Ferrage, E., Lanson, B., Michot, L.J. and Robert, J.-L. (2010) Hydration properties and interlayer organization of water and ions in synthetic Na-smectite with tetrahedral layer charge. Part 1. Results from X-ray diffraction profile modeling. *The Journal of Physical Chemistry C* 114, 4515-4526.

Gaboreau, S., Lerouge, C., Dewonck, S., Linard, Y., Bourbon, X., Fialips, C.I., Mazurier, A., Pret, D., Borschneck, D., Montouillout, V., Gaucher, E.C. and Claret, F. (2012) In-Situ Interaction of Cement Paste and Shotcrete with Claystones in a Deep Disposal Context. *Am J Sci* 312, 314-356.

García-Siñeriz, J.L., Abós, H., Martínez, V., De la Rosa, C., Mäder, U. and Kober, F., 2016. FEBEX DP: Dismantling of heater 2 at the FEBEX "in situ" test: Description of operations - Arbeitsbericht NAB 16-11, National Cooperative for the Disposal of Radioactive Waste (NAGRA), Wettingen, Switzerland.

Gates, W.P., Bouazza, A. and Churchman, G.J. (2009) Bentonite clay keeps pollutants at bay. *Elements* 5, 105-110.

Gómez-Espina, R. and Villar, M. (2016) Time evolution of MX-80 bentonite geochemistry under thermo-hydraulic gradients. *Clay Miner* 51, 145-160.

Greathouse, J.A., Cygan, R.T., Fredrich, J.T. and Jerauld, G.R. (2016) Molecular dynamics simulation of diffusion and electrical conductivity in montmorillonite interlayers. *The Journal of Physical Chemistry C* 120, 1640-1649.

Grim, R.E., 1968. Clay mineralogy. International series in the earth and planetary sciences. McGraw-Hill, New York.

Ho, T.A., Criscenti, L.J. and Wang, Y. (2016) Nanostructural control of methane release in kerogen and its implications to wellbore production decline. *Scientific reports* 6, 1-9.

Ho, T.A., Wang, Y. and Criscenti, L.J. (2018) Chemo-mechanical coupling in kerogen gas adsorption/desorption. *Phys Chem Chem Phys* 20, 12390-12395.

Ho, T.A., Criscenti, L.J. and Greathouse, J.A. (2019a) Revealing transition states during the hydration of clay minerals. *The journal of physical chemistry letters* 10, 3704-3709.

Ho, T.A. and Wang, Y. (2019b) Enhancement of oil flow in shale nanopores by manipulating friction and viscosity. *Phys Chem Chem Phys* 21, 12777-12786.

Ho, T.A., Wang, Y., Jové Colón, C.F. and Coker, E.N. (2020) Fast Advective Water Flow Through Nanochannels in Clay Interlayers: Implications for Moisture Transport in Soils and Unconventional Oil/Gas Production. *ACS Applied Nano Materials* 3, 11897-11905.

Hockney, R. and Eastwood, J. (1988) *Computer Simulation Using Particles* Taylor & Francis. Inc., USA.

Holmboe, M. and Bourg, I.C. (2014) Molecular dynamics simulations of water and sodium diffusion in smectite interlayer nanopores as a function of pore size and temperature. *The Journal of Physical Chemistry C* 118, 1001-1013.

Huertas, F., Fuentes-Cantillana, J.L., Jullien, F., Rivas, P., Linares, J., Fariña, P., Ghoreychi, M., Jockwer, N., Kickmaier, W., Martínez, M.A., Samper, J., Alonso, E. and Elorza, F.J., (2000) Full-scale engineered barriers experiment for a deep geological repository for high-level radioactive waste in crystalline host rock (FEBEX project): Final report. EUR 19147, European Commission, Brussels.

Jové Colón, C.F., Weck, P.F., Sassani, D.C., Zheng, L., Rutqvist, J., Steefel, C.I., Kim, K., Nakagawa, S., Houseworth, J., Birkholzer, J., Caporuscio, F.A., Cheshire, M., Rearick, M.S., McCarney, M.K., Zavarin, M., Benedicto-Cordoba, A., Kersting, A.B., Sutton, M., Jerden, J.L., Frey, K.E., Copple, J.M. and Ebert, W.L. (2014) Evaluation of Used Fuel Disposition in Clay-Bearing Rock (FCRD-UFD-2014-000056). Sandia National Laboratories, SAND2014-18303 R, Albuquerque, New Mexico, 434 pp.

Jové Colón, C.F., Payne, C., Coker, E., Boisvert, L., Sanchez, A., Knight, A. and Hadgu, T. (2019) Argillite Disposal R&D International Collaborations interim report - 2019 (SAND2019-6731 R), Prepared for U.S. Department of Energy (DOE) Spent Fuel Waste Science and Technology (SFWST). Sandia National Laboratories, Albuquerque, New Mexico, 51 pp.

Jové Colón, C.F., C. Payne, and A. Knight, 2018. International Collaboration Activities on Disposal in Argillite R&D: Progress Report, in Spent Fuel Waste Science and Technology Deliverable M4SF18SN010301092 (SAND2018-9718 R), Sandia National Laboratories: Albuquerque, New Mexico USA. p. 51.

Jové Colón, C.F., Hammond, G.E., Kuhlman, K., Zheng, L., Kim, K., Xu, H., Rutqvist, J., Caporuscio, F.A., Norskog, K.E., Maner, J., Palaich, S., Cheshire, M., Zavarin, M., Wolery, T.J., Atkins-Duffin, C., Jerden, J.L., Copple, J.M., Cruse, T. and Ebert, W.L., 2016. Evaluation of Used Fuel Disposition in Clay-Bearing Rock (FCRD-UFD-2016-000074), Sandia National Laboratories, Albuquerque, NM. SAND2016-10311 R.

Kosakowski, G. and Berner, U. (2013) The evolution of clay rock/cement interfaces in a cementitious repository for low- and intermediate level radioactive waste. *Phys Chem Earth* 64, 65-86. Hisatake, K., Tanaka, S. and Aizawa, Y. (1993) Evaporation rate of water in a vessel. *J Appl Phys* 73, 7395-7401.

Klein-BenDavid, O., Harlavan, Y., Levkov, I., Teutsch, N., Brown, K., Gruber, C. and Ganor, J. (2019) Interaction between spent fuel components and carbonate rocks. *Science of The Total Environment* 689, 469-480.

Lichtner, P.C., (2016) Kinetic rate laws invariant to scaling the mineral formula unit. *American Journal of Science*, 316(5): p. 437-469.

Lichtner, P. C., et al. (2019). PFLOTRAN user manual: A massively parallel reactive flow and transport model for describing surface and subsurface processes. <http://documentation.pflotran.org>

Liu, X., Lu, X., Wang, R. and Zhou, H. (2008) Effects of layer-charge distribution on the thermodynamic and microscopic properties of Cs-smectite. *Geochim Cosmochim Acta*, 72, 1837-1847.

Matteo, E.N., Dewers, T.A., Jove Colon, C.F., Hadgu, T., Gruber, C., Steen, M., Brown, K., Delapp, R., Brown, L. and Kosson, D. (2019) FY19 Progress of EBS International Collaborations. Sandia National Laboratories; M4SF-19SN010308082; SAND2019-10787 R, Albuquerque, NM USA, p. 38 pp.

Matteo, E., Dewers, T., Gomez, S., Hadgu, T., Zheng, L., Lammers, L.N., Fox, P., Chang, C., Xu, H., Borglin, S., Whittaker, M.L., Chou, C., Tournassat, C., Subramanian, N., Wu, Y., Nico, P., Gilbert, B., Kneafsey, T., Caporuscio, F.A., Sauer, K.B., Rock, M.J., Kalintsev, A., Migdisov, A., Alcorn, S., Buck, E.C., Yu, X.-Y., Yao, J., Son, J., Reichers, S.L., Klein-BenDavid, O., Bar-Nes, G., Meeussen, J.C.L., Gruber, C., Steen, M., Brown, K.G., Delapp, R., Taylor, A., Ayers, J. and Kosson, D.S. (2020) Evaluation of Engineered Barrier Systems FY20 Report. Sandia National Laboratories; M2SF-20SN010308042; SAND2020-11452 R, Albuquerque, NM USA.

Martinez, V., Abós, H. and García-Siñeriz, J.L., (2016) FEBEXe: Final Sensor Data Report (FEBEX "in situ" Experiment) - Arbeitsbericht NAB 16-19, National Cooperative for the Disposal of Radioactive Waste (NAGRA), Wettingen, Switzerland.

Marty, N.C., Bildstein, O., Blanc, P., Claret, F., Cochapin, B., Gaucher, E.C., Jacques, D., Lartigue, J.-E., Liu, S. and Mayer, K.U. (2015) Benchmarks for multicomponent reactive transport across a cement/clay interface. *Computat Geosci*, 1-19.

Marty, N.C., Grangeon, S., Lassin, A., Madé, B., Blanc, P. and Lanson, B. (2020) A quantitative and mechanistic model for the coupling between chemistry and clay hydration. *Geochim Cosmochim Acta* 283, 124-135.

Martyna, G.J., Tobias, D.J. and Klein, M.L. (1994) Constant pressure molecular dynamics algorithms. *The Journal of chemical physics* 101, 4177-4189.

McKay, J. (1992) Clay Separation. LSIS Technical Memorandum #92-1. University of Western Ohio.

Missana, T. and García-Gutiérrez, M. (2007). Sorption of bivalent ions (Ca (II), Sr (II) and Co (II)) onto FEBEX bentonite. *Physics and Chemistry of the Earth, Parts A/B/C*, 32(8): 559-567.

Montes-H, G., J. Duplay, L. Martinez, Y. Geraud, and B. Rousset-Tournier (2003) Influence of interlayer cations on the water sorption and swelling–shrinkage of MX80 bentonite. *Applied Clay Science*, 23(5-6): p. 309-321.

Morodome, S. and Kawamura, K. (2009) Swelling behavior of Na-and Ca-montmorillonite up to 150 C by in situ X-ray diffraction experiments. *Clay Clay Miner* 57, 150-160.

Morrow, C.P., Yazaydin, A.O.z.r., Krishnan, M., Bowers, G.M., Kalinichev, A.G. and Kirkpatrick, R.J. (2013) Structure, energetics, and dynamics of smectite clay interlayer hydration: Molecular dynamics and metadynamics investigation of Na-hectorite. *The Journal of Physical Chemistry C* 117, 5172-5187.

Moyne, C. and Murad, M.A. (2002) Electro-chemo-mechanical couplings in swelling clays derived from a micro/macro-homogenization procedure. *Int J Solids Struct* 39, 6159-6190.

Muurinen, A. (2011) Measurements on Cation Exchange Capacity of Bentonite in the Long-Term Test of Buffer Material (LOT), Working Report 2011-10. POSIVA, Eurajoki, Finland, pp. 30.

Nair, R., Wu, H., Jayaram, P., Grigorieva, I. and Geim, A. (2012) Unimpeded permeation of water through helium-leak-tight graphene-based membranes. *Science* 335, 442-444.

Neek-Amal, M., Peeters, F.M., Grigorieva, I.V. and Geim, A.K. (2016) Commensurability effects in viscosity of nanoconfined water. *ACS nano* 10, 3685-3692.

Ngouana W, B.F. and Kalinichev, A.G. (2014) Structural arrangements of isomorphic substitutions in smectites: Molecular simulation of the swelling properties, interlayer structure, and dynamics of hydrated Cs–montmorillonite revisited with new clay models. *The Journal of Physical Chemistry C* 118, 12758-12773.

Nosé, S. (1984) A molecular dynamics method for simulations in the canonical ensemble. *Molecular physics* 52, 255-268.

Ortiz-Young, D., Chiu, H.-C., Kim, S., Voitchovsky, K. and Riedo, E. (2013) The interplay between apparent viscosity and wettability in nanoconfined water. *Nature communications* 4, 1-6.

Plimpton, S. (1995). "Fast Parallel Algorithms for Short-Range Molecular Dynamics." *J Comp Phys* 117: 1-19.

Pouvreau, M., Greathouse, J.A., Cygan, R.T. and Kalinichev, A.G. (2017) Structure of hydrated gibbsite and brucite edge surfaces: DFT results and further development of the clayFF classical

force field with metal–O–H angle bending terms. *The Journal of Physical Chemistry C* 121, 14757-14771.

Pouvreau, M., Greathouse, J.A., Cygan, R.T. and Kalinichev, A.G. (2019) Structure of hydrated kaolinite edge surfaces: DFT results and further development of the ClayFF classical force field with metal–O–H angle bending terms. *The Journal of Physical Chemistry C* 123, 11628-11638.

Radha, B., Esfandiar, A., Wang, F., Rooney, A., Gopinadhan, K., Keerthi, A., Mishchenko, A., Janardanan, A., Blake, P. and Fumagalli, L. (2016) Molecular transport through capillaries made with atomic-scale precision. *Nature* 538, 222-225.

Rotenberg, B., Marry, V., Vuilleumier, R., Malikova, N., Simon, C. and Turq, P. (2007) Water and ions in clays: Unraveling the interlayer/micropore exchange using molecular dynamics. *Geochim Cosmochim Acta*, 71, 5089-5101.

Smith, D.E. and Dang, L.X. (1994) Computer simulations of NaCl association in polarizable water. *The Journal of Chemical Physics* 100, 3757-3766.

Soler, J.M. (2012) High-pH plume from low-alkali-cement fracture grouting: Reactive transport modeling and comparison with pH monitoring at ONKALO (Finland). *Appl Geochem* 27, 2096-2106.

Soler, J.M. and Mader, U.K. (2010) Cement-rock interaction: Infiltration of a high-pH solution into a fractured granite core. *Geologica Acta* 8, 221-233.

Sun, L., Hirvi, J.T., Schatz, T., Kasa, S. and Pakkanen, T.A. (2015) Estimation of montmorillonite swelling pressure: A molecular dynamics approach. *The Journal of Physical Chemistry C* 119, 19863-19868.

Tamura, K., Yamada, H. and Nakazawa, H. (2000) Stepwise hydration of high-quality synthetic smectite with various cations. *Clay Clay Miner* 48, 400-404.

Teich-McGoldrick, S.L., Greathouse, J.A., Jové-Colón, C.F. and Cygan, R.T. (2015) Swelling Properties of Montmorillonite and Beidellite Clay Minerals from Molecular Simulation: Comparison of Temperature, Interlayer Cation, and Charge Location Effects. *The Journal of Physical Chemistry C*, 119(36): 20880-20891.

Teleman, O., Jönsson, B. and Engström, S. (1987) A molecular dynamics simulation of a water model with intramolecular degrees of freedom. *Molecular Physics* 60, 193-203.

U.S. EPA (2017) SW-846 Test Method 1315: Mass Transfer Rates of Constituents in Monolithic or Compacted Granular Materials Using a Semi-Dynamic Tank Leaching Procedure, Washington, D.C.

Villar, M.V., Fernandez, A.M., Romero, E., Dueck, A., Cuevas, J., Plotze, M., Kaufhold, S., Dohrmann, R., Iglesias, R.J., Sakaki, T., Voltolini, M., Zheng, L., Kawamoto, K. and Kober, F. (2017) FEBEX-DP Post-mortem THM/THG Analysis Report, NAGRA Arbeitsbericht NAB 16-17. NAGRA, Wettingen, Switzerland, pp. 187 pp.



Vinci, Doriana, Baptiste Dazas, Eric Ferrage, Martine Lanson, Valérie Magnin, Nathaniel Findling, and Bruno Lanson (2020) "Influence of layer charge on hydration properties of synthetic octahedrally-charged Na-saturated trioctahedral swelling phyllosilicates." *Applied Clay Science* 184: 105404.

Wang, Y., T. Hadgu, E. A. Kalinina, J. Jerden, V. K. Gattu, W. Ebert, H. Viswanathan, J. Hyman, S. Karra, N., Knapp, N. Makedonska, P. Reimus, K. Telfeyan, P. M. Fox, P. S. Nico, M. Zavarin, E. Balboni, and C. Atkins-Duffin: Evaluation of Spent Fuel Disposition in Crystalline Rocks: FY17 Progress Report, Spent Fuel and waste Disposition, SFWD-SFWST-2017-000007, September, 2017.

Wilson, J.C., Benbow, S., Sasamoto, H., Savage, D. and Watson, C. (2015) Thermodynamic and fully-coupled reactive transport models of a steel-bentonite interface. *Applied Geochemistry*.

Xie, M.L., Mayer, K.U., Claret, F., Alt-Epping, P., Jacques, D., Steefel, C., Chiaberge, C. and Simunek, J. (2015) Implementation and evaluation of permeability-porosity and tortuosity-porosity relationships linked to mineral dissolution-precipitation. *Computat Geosci* 19, 655-671.

Yamada, H., Nakazawa, H., Hashizume, H., Shimomura, S. and Watanabe, T. (1994) Hydration behavior of Na-smectite crystals synthesized at high pressure and high temperature. *Clay Clay Miner* 42, 77-80.

Ye, H., Zhang, H., Zhang, Z. and Zheng, Y. (2011) Size and temperature effects on the viscosity of water inside carbon nanotubes. *Nanoscale research letters* 6, 1-5.